

**Department of Physics and Astronomy**  
**University of Heidelberg**

Bachelor Thesis in Physics  
submitted by

**Katja Beckerle**

born in Mannheim (Germany)

**2012**



# **Ionization of Osmium in a Stellar Plasma under s-Process Conditions**

This Bachelor Thesis has been carried out by Katja Beckerle at the  
Max Planck Institute for Nuclear Physics in Heidelberg  
under the supervision of  
Dr. Adriana Pálffy  
and  
Prof. Dr. C. H. Keitel

*You can get it if you really want.<sup>1</sup>*

---

<sup>1</sup>Jimmy Cliff

## Abstract

The charge state distribution of ions of a heavy nuclei species in the stellar plasma environment in which they were formed by s-process nucleosynthesis is investigated. Our aim is to gain insight about the atomic inner-shell electron occupation of heavy elements. The vacancy of the inner shells are of interest when evaluating the role of electronic recombination processes like nuclear excitation by electron capture in s-process nucleosynthesis. To this end we investigate the ionization of osmium ( $Z=76$ ) as a test case in stellar plasma conditions relevant for the formation of heavy nuclei. For these parameters we derive the ionization states that are formed with the help of the Saha equation. The potential generated by the plasma electrons and ions is treated in the framework of the Fermi model including quantum mechanical corrections. The latter is used to obtain the reduction of the atomic binding energies and the correction of the partition functions due to the plasma particles. Our results predict free K and nearly free L shells for osmium for various plasma parameter sets typical for the s-process sites. These findings support the further study of nuclear excitation by electron capture in stellar plasmas, given that the former is strongly facilitated when recombination in inner shells is possible.

## Zusammenfassung

In dieser Arbeit wird der Ionisierungsgrad von Osmium in einem stellaren Plasma untersucht, in welchem das Ion zuvor über die s-Prozess Nukleosynthese gebildet wurde. Hierdurch soll die Besetzung der inneren Elektronenschalen für schwere Elemente bestimmt werden, die von großer Bedeutung für die Rolle elektronischer Rekombinationsprozesse wie der Kernanregung durch Elektroneneinfang für hoch angeregte Kerne bei der Entstehung neuer Elemente ist. Die Ionisierungsgrade des gewählten Testions Osmium ( $Z=76$ ) werden mit Hilfe der Saha Gleichung für diejenigen Parameter berechnet, die das bei s-Prozess Nukleosynthese schwerer Isotope vorliegende Plasma am besten beschreiben. Um das Ladungspotential der das Ion umgebenden Plasmapartikel einzubeziehen, wenden wir ein quantenmechanisch korrigiertes Fermi Modell an. Mit Hilfe dieses Potentials können wir die durch die Plasmapartikel verursachte Verringerung der Bindungsenergien der gebundenen Elektronen und damit den maximalen Anregungsenergiewert berechnen, der innerhalb der Zustandssumme für das Osmiumion Berücksichtigung findet. Im Ergebnis stellen wir fest, dass die K-Schalen und partiell auch die L-Schalen des Osmium für die gewählten Plasmaparameter unbesetzt sind. Damit zeigen wir die Notwendigkeit weiterer Untersuchung der bei Rekombination in innere Schalen besonders effektiven Kernanregung durch Elektroneneinfang in stellaren Plasmen.



# Contents

<b>1</b>	<b>Introduction</b>	<b>5</b>
<b>2</b>	<b>S-Process Nucleosynthesis</b>	<b>8</b>
2.1	Neutron Capture Process . . . . .	8
2.2	S-Process . . . . .	9
2.3	$^{187}\text{Os}$ and the Os/Re Clock . . . . .	10
2.4	Physical Sites . . . . .	11
<b>3</b>	<b>Degree of Ionization in the Plasma</b>	<b>14</b>
3.1	Derivation of the Saha Equation . . . . .	14
3.2	Chemical Potential . . . . .	17
3.3	Continuum Depression . . . . .	18
3.3.1	Non-Relativistic Case . . . . .	19
3.3.2	Relativistic Calculation . . . . .	27
<b>4</b>	<b>Numerical Results for Os</b>	<b>33</b>
4.1	Self-Consistent Method . . . . .	33
4.1.1	Approximations Within the Saha Equation . . . . .	33
4.1.2	Detailed Calculation For One Configuration . . . . .	34
4.1.3	Results For All Configurations . . . . .	40
4.2	Comparison With Values From the Literature . . . . .	42
	<b>Summary and Outlook</b>	<b>44</b>





# 1 Introduction

The mechanism of element formation has riddled generations of scientists beginning with the first half of the twentieth century. It is known by now that the synthesis of all elements heavier than iron takes place in stars. Since iron is the stable nucleus with the highest binding energy, heavier elements cannot be produced by exothermal fusion processes of other lighter nuclei. Instead they are essentially formed by the absorption of neutrons and to a much lesser extent by proton capture. That neutron capture on heavy nuclei occurs is due to the electrical neutrality of neutrons, which ensures that the charge of the nuclei presents no barrier for the capture process. The formed neutron-rich nuclei are unstable and usually undergo  $\beta$  decay. Two modes for neutron capture can be distinguished by its occurrence rate with regard to  $\beta$  decay of the nucleus: the slow (s-process) and the rapid (r-process) neutron capture process [BBFH57]. The r-process is ascribed to explosive conditions as in supernovae, where the neutron flux is so high that many neutrons can be captured by a nucleus, prior to its decay. The s-process is characterized by a lower neutron flux over a long period of time, where an unstable nucleus after neutron absorption decays before another capture process may occur. For a long time following the original hypothesis concerning the s-process, its underlying physical sites were only vaguely defined, since the conditions—high thermal energy over a long period of time—are too extreme to be replicated in a laboratory. Meanwhile, much progress has been made, mostly due to astronomical observations of stars and measurement of their element abundances. However, many questions are not answered yet, and most studies of the s-process still rely on a variety of assumptions and approximations.

Among other things, the role played by excited nuclear states in s-process nucleosynthesis has not fully been clarified. The excitation of nuclear states may modify the decay rates and change the ratio of the possible nuclear decay channels as presented in Ref. [GM04, GMM07, GMM10]. For the low-lying excited states, thermal equilibrium of the nuclear states population can be assumed. To account for the change in the nuclear cross section, the stellar enhancement factor (SEF) has been introduced. It gives a value for the ratio of an effective cross section for a thermally equilibrated nucleus and the corresponding Maxwellian averaged ground state cross section [BBK<sup>+</sup>00]. Such a convenient treatment is not possible for the high-lying nuclear excited states close to the neutron threshold, as they are too short lived to allow the assumption of thermodynamic equilibrated conditions. A stellar plasma is the typical physical site where such highly excited nuclear states are likely to be formed via neutron capture. Such processes were treated by Bernstein [BBB<sup>+</sup>] with respect to the study of photon absorption on massive neutron-rich nuclei in plasma conditions resembling the r-process sites and its influence on the decay rates and neutron-induced fission. It was shown that immediately after neutron capture, photoabsorption can lead to a substantial change in the decay channel branching ratio of the compound nucleus. However, hot dense stellar plasmas exhibit not only a high density of photons, but also a vast number of (free) electrons, whose inclusion in considerations of absorption, recombination and decay processes is called for. Recently, the impact of an electron recombination process on highly excited nuclear states under s-process conditions was considered by Helmrich in Ref. [Hel11]. In detail, nuclear excitation by electron capture (NEEC) occurring on compound nuclei immediately following neutron absorption was investigated.

NEEC denotes the resonant process of electron capture into a vacancy of the atomic shell with direct and simultaneous excitation of the nucleus [PSH06]. The whole process of NEEC followed by the deexcitation of the nucleus, with its initial, resonant and final state is displayed in Figure

1.1. The initial state (i) refers to the ion before the occurrence of NEEC, where the nucleus is in its ground state (G). Additionally, the L-shell is free, so that electron capture can take place. The resonant state (d) formed via NEEC is depicted in the central picture. The continuum electron recombines into the L shell transferring its surplus energy to the nucleus that reaches the excited state E. The last picture then shows the final state (f), where the nucleus deexcites via photon emission.

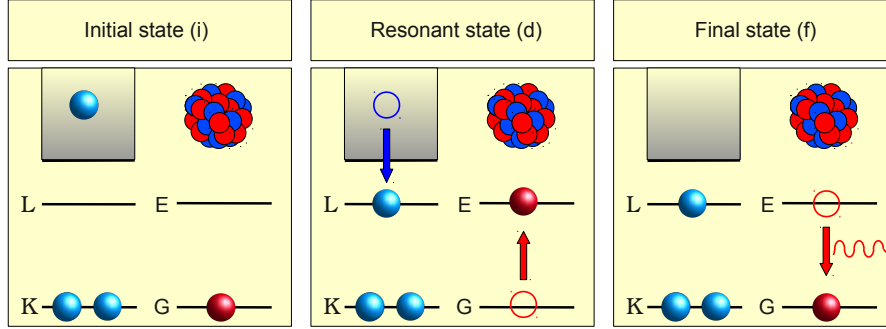


**Figure 1.1:** Schematic illustration of nuclear excitation by electron capture. The electron capture process is depicted on the left hand side of every picture, the nuclear excitation process on the right hand side. The three pictures depict the three states of the process: the first shows an atom with a free L-shell and a nucleus in its ground state (initial state i); the second illustrates the capture process with simultaneous nuclear excitation (resonant state d) and the third corresponds to the final state (f), where the nucleus has already decayed via photon emission.

The cross section for NEEC on a ground state nucleus in connection with its radiative decay as a two-step process has been derived by Pálffy in [P06]. Based on this work, a two-step process cross section has been developed further to account for NEEC on highly excited nuclear states after s-process neutron capture (and before deexcitation via  $\gamma$  decay) under simplified characteristic stellar plasma conditions by Helmrich [Hel11]. Since for an already highly excited nucleus the even higher lying discrete excitation levels are energetically closer together, even NEEC with transition energies on the order of tens of keV is supposed to be efficient. In Ref. [Hel11] it was shown that the impact of NEEC can be substantial enough to significantly change the net decay rates of the compound nucleus. In the absence of NEEC,  $\gamma$  decay is more likely to occur than neutron reemission, such that the formation of heavier isotopes is probable. In contrast, with NEEC the neutron reemission is enhanced and can even dominate over the  $\gamma$  decay. This suppresses the production of daughter isotopes. The possible impact of this result makes it worthwhile to address this subject in more detail.

In Ref. [Hel11], various simplifying assumptions and approximations were made in order to obtain a first rough estimate of the effect. However, it is indispensable to investigate the validity of these assumptions for the results to hold, especially when it comes to properly taking into account the actual physical conditions of the process. One such assumption is that under s-process conditions the electron capture occurs into the K- and L-shells of the chosen model isotopes  $^{187}\text{Os}$ . The impact of NEEC on s-process nucleosynthesis was estimated in Ref. [Hel11] by taking into account only recombination in these atomic shells, which present the largest NEEC cross sections and are thus of greatest relevance.

The aim of this work is now to verify the assumption that the K- and L-shells of the  $^{187}\text{Os}$  isotopes are indeed vacant. This would be true if most osmium were present in ionization states with less bound electrons than are needed to fill the K- and L-shells. As data for ionization states

---

of heavy isotopes in dense stellar plasmas is not generally available, we need to derive theoretical values for the ionization degree. To this end we consider plasma conditions characteristic for s-process nucleosynthesis and calculate probabilities for various charged states and ionization stages of osmium with the help of the Saha equation. Additionally, we account for the influence of the plasma particles on the binding potential via a Fermi model for free electrons modified by a quantum mechanical correction to account for the discrete bound electron states of the ion. Since the calculations in Ref. [Hel11] were done for  $^{187}\text{Os}$ , we also adopt this isotope as our model ion. As part of a galactic chronometer that uses mass abundance ratios to evaluate the age of our galaxy,  $^{187}\text{Os}$  is of special interest and is often discussed in the literature. However, as far as the ionization states of  $^{187}\text{Os}$  in an s-process environment are concerned, the data is scarce and we are only aware of Ref. [TY83] that investigated the impact of bound-state  $\beta$  decay for ionized osmium in a nucleosynthesis scenario. This work considers two plasma configuration parameter sets with few chemical constituents and presents only limited data regarding the osmium ionization states. Furthermore, the chosen chemical mixtures are not an accurate representative of the s-process environment. We have therefore used Ref. [TY83] only for a comparison and double-check of our calculation method.

To make more realistic predictions for the required ionization states we investigate the s-process conditions in more detail and have a closer look at the processes in the respective stellar sites. This enables us to determine the most probable plasma configurations and extract the parameters needed to perform our calculation of the ionization states. The environment of our osmium ion we show to consist primarily of helium with a large mass-fraction carbon and a smaller abundance of oxygen. The temperatures range from  $0.9 \cdot 10^8$  K to  $3 \cdot 10^8$  K. We adopt not only these parameters but also include two more plasma compositions and an even higher temperature to account for traditional s-process plasma treatment and to allow a comparison with literature values.

Our results demonstrate that there is always a vacant place within the L-shell of the osmium ion. Most likely also the K-shell is free for an electron to be captured in. The investigated plasma conditions cause the osmium isotope to be highly ionized, leaving only between six and one bound electron depending on the temperature that we ascribe to the s-process.

This thesis is structured as follows: In chapter 2 we will give an introduction to nucleosynthesis and explain in more detail the possible impact of NEEC. Additionally, we will address the special role of  $^{187}\text{Os}$  within the nucleosynthesis studies and portray the physical sites of the s-process nucleosynthesis describing the plasma conditions that we assume in our calculations. Thereafter we will give detailed information concerning our computation method for the ionization states under consideration of the plasma effects in chapter 3. Our numerical results will be shown in chapter 4 where we will calculate the occurring ionization states for the possible plasma conditions. The work concludes with a summary and outlook of possible future directions of study.

## 2 S-Process Nucleosynthesis

In the following we present the frame for our calculations. First we portray the basic nuclear process. Afterwards we describe the importance of the chosen model isotope and outline the physical sites in which the respective process takes place. This results in certain plasma conditions which we need to consider as we proceed with the calculation of the ionization states.

### 2.1 Neutron Capture Process

Of the various elements in our periodic system, hydrogen was formed shortly after the Big Bang. Much later, nuclear processes in stars were responsible for the synthesis of all elements heavier than hydrogen [KBW89]. Whereas elements up to the iron peak (mass number  $A$  from 50 to 65 [Ili07]), who exhibit the highest binding energies per nucleon, are produced via exothermal fusion processes - mainly in massive stars -, heavier elements are not synthesized by charged particle reactions (with the exception of the supposedly small effect of proton capture on neutron rich isotopes) due to the increased Coulomb barrier. The proton rich nuclei repel each other and fusion is not energetically favorable. Instead heavier elements are produced by neutron capture with the emission of  $\gamma$ -radiation ( $n, \gamma$ ) and subsequent  $\beta$ -decay processes. Depending on the time scale on which neutron capture occurs, two modes can be distinguished:

- If basically every neutron capture ( $n, \gamma$ ) that leads to an instable nucleus is followed by  $\beta$  decay, one speaks of the s(low)-process [BBFH57]. Compared to  $\beta$  decay, the neutron capture occurs on a slow rate. Inevitably, its path runs along the group of  $\beta$ -stable nuclides whose typical  $\beta^-$ -decay lifetimes range from minutes to years. The neutron flux at s-process sites amounts to about  $N_n \approx 10^8 \text{cm}^{-3}$  [Ili07].
- At the other end, the process of neutron capture on a very short time-scale (from seconds to minutes) under explosive conditions is called r(apid)-process [BBFH57, KGBA11]. As its name indicates, here the neutron capture process occurs very fast compared to the  $\beta$ -decay lifetimes.

The r-process is facilitated by high neutron abundances ( $N_n \approx 10^{21} \text{cm}^{-3}$ ) and runs close to the neutron drip line [Ili07]. The nuclei absorb neutrons until the neutron flux terminates. Then, successive  $\beta^-$  decay leads to the next possible, thus most neutron-rich stable or very long-lived isobar. This isobar might shield another isobar with higher proton number  $Z$  and lesser neutron number  $N_n$ , which then can only be reached via the s-process (called s-only isobar). The product of the s-process have more balanced  $Z$  and  $N_n$  numbers [BBFH57].

In Figure 2.1 we present schematically the neutron capture nucleosynthesis paths. The neutron capture processes start from mainly the abundant iron (Fe) isotope. The s-process continues smoothly up to the most massive stable nucleus  $^{209}\text{Bi}$ , where any other neutron capture results in the occurrence of  $\alpha$  decay. The only slight discontinuities appear as magic peaks [BBFH57], where  $\beta^-$  decay takes a long time due to a relative stability at the neutron magic numbers  $N_n = 50$  and  $N_n = 82$ . The completeness of the respective nuclear shell in this cases with its high binding energy exhibits very small cross sections and prevents further neutron capture [KBW89]. Consequently those isotopes are the most abundant ones within the s-process, besides the ones right before the neutron magic number  $N_n = 126$ , that lies however past the s-process termination point at bismuth. The abundance peaks at magic numbers are more pronounced for the isotopes produced via the r-process. There the capture of neutrons stops not only when the

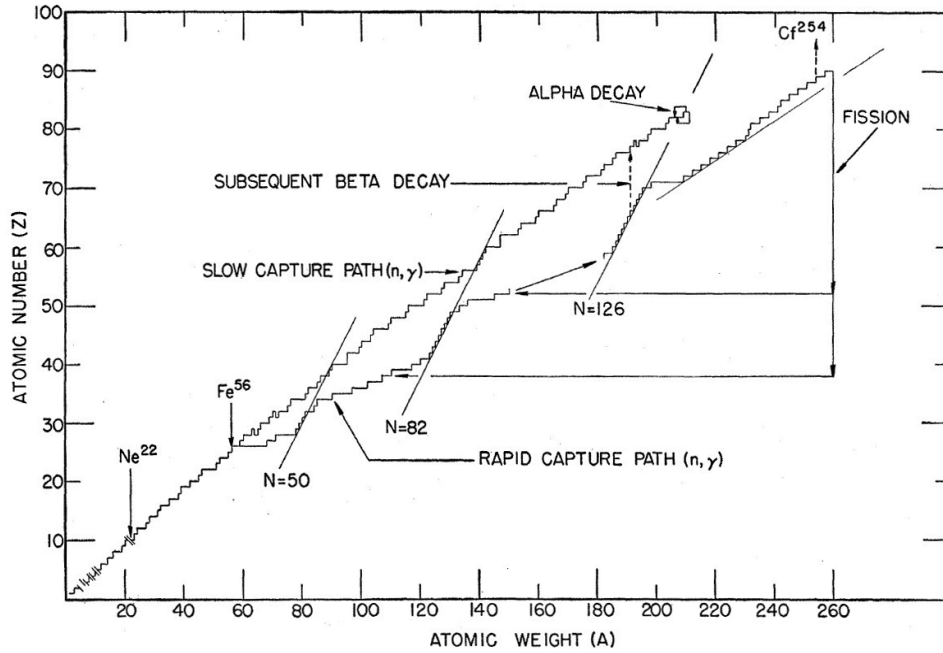


**Figure 2.1:** The neutron capture paths of the s- and r-process. Reproduced from [BBFH57].

neutron flux decreases, but also when the binding energy becomes as low as 2 MeV. This is the case at large distances from the stability line in the  $A$  to  $Z$  plane after the three identified magic neutron numbers [BBFH57]. Before another neutron can be added,  $\beta^-$  decay has to take place, bringing the isobars closer to the stability line in a staircase pattern. The r-process builds up heavier isotopes than the s-process, but at an atomic mass number of about 260 the neutrons induce fission, which leads the resulting isotopes back into the neutron synthesis chain.

During the neutron capture process—right after the neutron absorption—for a very short time a compound nucleus is formed. In such a situation subsequent NEEC (nuclear excitation by electron capture) of even only a few keV can have a significant effect and change the net decay rates of the compound nucleus. To illustrate the possible effect of NEEC, in Figure 2.2 the normal neutron capture process with the two deexcitation modes neutron reemission and  $\gamma$  decay is set in contrast to the scenario of NEEC occurring before deexcitation.

## 2.2 S-Process

The s-process can be divided into three principal parts: first there is the weak s-process component, which leads to isotopes with atomic mass numbers from  $A = 22$  to  $A = 50$ . Above  $A = 205$ , the s-process is denoted as its strong component; the mass numbers in between are composed through the so called main s-process component [Ili07]. The components are also separated by their different development conditions.

The path of the s-process is not always well-defined. Instead there exist about 15 to 20 significant branching points [Ili07] which reflect the surrounding conditions. A branching point is a certain isotope starting from which the s-process can continue via two different paths. Two mechanism influence the course after the branching points. First, higher temperature might lead to the population of excited nuclear states and in some cases of metastable isomers of the branching point isotope with longer or shorter half-lives [GM04, GMM07]. Whereas the ground state atom might capture another neutron, the isomer might  $\beta$  decay to the  $(Z + 1)$ -isotope,

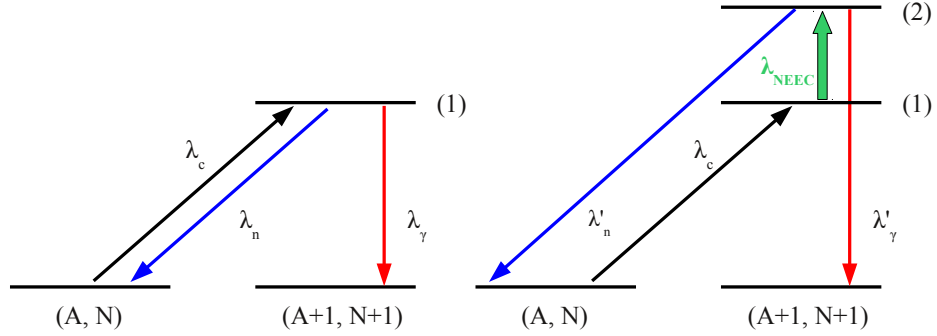


**Figure 2.2:** Schematic illustration of the neutron capture process with the subsequent neutron reemission and  $\gamma$ -decay modes (left), and neutron capture followed by NEEC before it deexcites via the same two decay channels (right).  $\lambda_c$  stands for the rate with which the compound nucleus is formed (neutron capture rate),  $\lambda_n$  denotes the neutron reemission rate,  $\lambda_\gamma$  the  $\gamma$ -decay rate and  $\lambda_{\text{NEEC}}$  the rate for the occurrence of NEEC. The prime marks a modified rate. The first excitation due to neutron absorption lifts the nucleus into excitation level (1), the NEEC accounts for the additional excitation from level (1) to level (2).

starting another s-process path. One example for this constellation is the  $^{79}\text{Se}$  branch [KK88]. Also branchings can occur where the  $\beta$ -decay half-life competes with the neutron capture rate (for example the  $^{85}\text{Kr}$  branch) depending on whether the neutron flux is high enough for the neutron capture to happen first [KGBA11]. Consequently the ratio of the elements after the branching points carry information about the stellar temperature and neutron flux. In the following we address the formation of the stable isotope  $^{187}\text{Os}$ , which lies on the main s-process path.

## 2.3 $^{187}\text{Os}$ and the Os/Re Clock

The  $^{187}\text{Os}$  isotope was primarily chosen as model isotope for the impact of NEEC in nucleosynthesis scenarios in [Hel11], because of its role as (nearly) s-only isotope that is part of the Re/Os-clock used for galactic age estimates. The Os/Re clock relies on the long-lived  $^{187}\text{Re}$  isotope with a half-life of 41.2 Gyr as a timer for the age of the galaxy. The s- and r-formation paths are depicted in Figure 2.3.

Both  $^{185}\text{W}$  and  $^{186}\text{Re}$  act as branching points in the s-process. Neutron capture transforms them into  $^{186}\text{W}$  and  $^{187}\text{Re}$ , while  $\beta$  decay instead leads to  $^{185}\text{Re}$  and  $^{186}\text{Os}$ , respectively. The latter continue in the main s-process path, meaning  $^{185}\text{Re}$  will capture a neutron proceeding as  $^{186}\text{Re}$ , and  $^{186}\text{Re}$  accordingly turns into  $^{186}\text{Os}$ , which itself as a stable isotope captures another neutron to become  $^{187}\text{Os}$  and so on. If the neutron capture succeeds, the following processes can hardly ever lead the isotope chain back to the main s-process path around  $^{187}\text{Os}$  to influence its abundance.  $^{186}\text{W}$  is stable and  $^{187}\text{Re}$  has a half-life of 41.2 Gyr. Both isotopes have a shielding function towards  $^{186}\text{Re}$  and  $^{187}\text{Os}$ , respectively, which are therefore s-only isotopes together with  $^{186}\text{Os}$ . Regarding  $^{187}\text{Os}$  this notation has limited validity since  $^{187}\text{Re}$  is only close to stable, and  $\beta$  decays with the half-life of 41.2 Gyr. The fraction of  $^{187}\text{Os}$  abundance that results from  $^{187}\text{Re}$  decay can therefore be determined by the total amount minus the s-process component  $N_s(^{187}\text{Os})$ , which can be computed via the ratio  $\frac{\langle\sigma\rangle(^{186}\text{Os})}{\langle\sigma\rangle(^{187}\text{Os})}N_s(^{186}\text{Os})$ , where  $\langle\sigma\rangle$  is the Maxwellian averaged (n,  $\gamma$ ) cross section at the stellar site.

Essentially,  $^{187}\text{Re}$  is produced via the r-process [BFF<sup>+</sup>96]. Because of its long half-life it constitutes a cosmochronometer, i.e., a galactic clock. The solar system abundance ratio of  $^{187}\text{Re}$  to  $^{187}\text{Os}$  with subtraction of the s-process path abundance of  $^{187}\text{Os}$  and other slight corrections

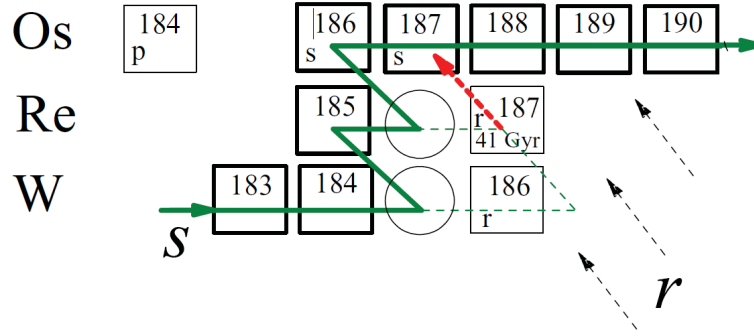


**Figure 2.3:** Sequence of the main s-process path (thick solid green line) including the branching points  $^{185}\text{W}$  and  $^{186}\text{Re}$  (circles); the thick red dashed arrow symbolizes the possible  $\beta^-$  decay of  $^{187}\text{Re}$ , the thin dashed arrows the r-process contribution. The small “r” stands for (nearly) r-only nuclei. Reproduced from [MFM<sup>+</sup>10].

delivers the age of the galaxy [SUM<sup>+</sup>05] or more precisely the time span since supernova explosions of the quickly evolved massive stars where r-process took place. An advantage here is that rhenium as well as osmium are siderophile elements, meaning they have the strong tendency to bond with metallic iron. The abundance ratio can therefore be extracted from meteorite samples [Cla64].

Adjustments to the known half-life of  $^{187}\text{Re}$  have been made in the last decades. Since in a stellar plasma highly ionized states are most likely, bound-state  $\beta^-$  decay has to be considered. In [BFF<sup>+</sup>96] the lifetime of the fully ionized  $^{187}\text{Re}$  was experimentally determined to be  $32.9 \pm 2.0$  yr. This work showed that the decay rate of  $^{187}\text{Re}$  is enhanced in stellar interiors, especially due to the  $\beta^-$  decay into the first excited bound state of  $^{187}\text{Os}$  [TY83]. The corresponding uncertainty of the Os/Re clock was amounted to 2 – 4 Gyr [FMM<sup>+</sup>10].

Further analysis concerning the pure s-process fraction of  $^{187}\text{Os}$  was performed. Especially, the Maxwell-averaged  $\langle n, \gamma \rangle$  cross section  $\langle \sigma \rangle$  was shown to be modified by the population of the low lying excitation levels of  $^{187}\text{Os}$  due to the equilibrium at stellar conditions. This situation is accounted for by the so called stellar enhancement factor [BBK<sup>+</sup>00]. However, the corresponding change in the neutron capture cross section affects the Re/Os clock to a minor extent (less than 1 Gyr) [FMM<sup>+</sup>10, SUM<sup>+</sup>05].

NEEC of  $^{187}\text{Os}$  after neutron capture can change the ratio of neutron reemission to deexcitation via  $\gamma$  decay which in turn may influence the measurable abundance of  $^{187}\text{Os}$  and of  $^{186}\text{Os}$  and therefore the Os/Re clock. In order to give a quantitative estimate of this effect, we need a more precise picture of the osmium ionization state in the nucleosynthesis plasma and therefore the plasma condition in which NEEC may occur. We address in the following the s-process sites and plasma conditions.

## 2.4 Physical Sites

The assumptions concerning the physical sites that host the s-process have been subject to historical development. The classical s-process described in Ref. [BBFH57] does not detail about the neutron sources and assumes a constant neutron density and temperature. Since then progress has been made due to a variety of data from astronomical observations, the development of stellar model codes, improved nuclear physics input, especially concerning the research on the

branching points, and the synergy between nuclear physics and other physics areas [KGBA11]. Now the weak component is ascribed to massive stars with mass  $M > M_{\odot}$  ( $M_{\odot}$  being the mass of the sun) whereas low-mass ( $1.5\text{--}3 M_{\odot}$ ) thermally pulsing asymptotic giant branch (TP-AGB) stars are considered to be responsible for the strong and main component [Son04]. The latter is of interest for us, since it comprises the formation of  $^{187}\text{Os}$ .

From the inside to the outside TP-AGB stars are composed of a compact core, which consists of carbon and oxygen, a helium burning shell, a thin helium intershell, a hydrogen burning shell and an extended hydrogen-rich envelope [CSG<sup>+</sup>09]. A crude schematical sketch - without the thin He intershell - is shown in Figure 2.4. Most of the time the H shell burning provides the

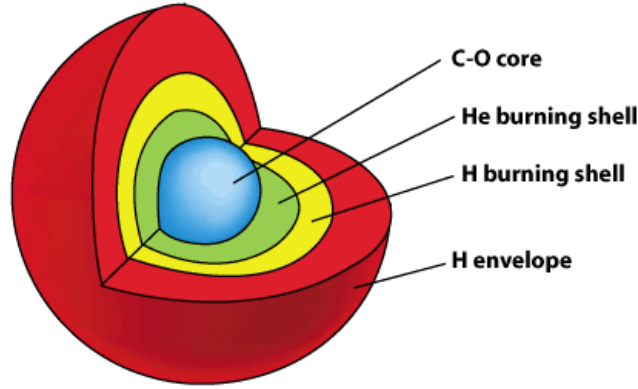


**Figure 2.4:** Composition of a TP-AGB star. Reproduced from [AGB12].

energy irradiated by the AGB stars and produces helium. Since the pressure of the H shell does not suffice to counteract the rise of the temperature through expansion, after a long time (about 10,000 to 100,000 years) the enriched He shell ignites. Due to the production of  $^{12}\text{C}$  via a triple- $\alpha$  reaction a huge amount of energy is released. This leads to a vast expansion of the He shell that extinguishes the H burning in the stretched H shell. During such a quasiexplosive thermal pulse not only a large amount of  $^{12}\text{C}$  is produced but also convection is driven in the whole intershell [KGBA11]. As a result the He intershell is enriched with C and heavy elements from the so-far occurred s-process [CSG<sup>+</sup>09]. After such a pulse the expansion subsides and the H shell reignites. This scenario repeats itself for several times. After a few thousand years of this radiatively He burning and a limited number of thermal pulses, the convective envelope penetrates into the top region of the C-rich He intershell zone mixing material to the surface. This is historically named *third dredge-up* [GAB<sup>+</sup>98]. When retreating from the surface a so-called  $^{13}\text{C}$  pocket is left behind, because some protons from the H-rich envelope are brought into the top layers of the He intershell [KGBA11]. There they are captured by the  $^{12}\text{C}$  and initiate the sequence  $^{12}\text{C}(\text{p},\gamma)^{13}\text{Ne}(\beta^+,\nu)^{13}\text{C}$  that forms the  $^{13}\text{C}$  pocket [Ili07], see Figure 2.5. Due to the large concentration of  $^{13}\text{C}$  within this pocket, a slow but high enough neutron flux can be provided by the reaction between the  $^{13}\text{C}$  and alpha particles to give rise to the s-process nucleosynthesis [GAB<sup>+</sup>98]. This process starts at a temperature of about  $T \sim 0.9 \cdot 10^8$  K. When it exceeds  $2.7 \cdot 10^8$  K also the  $^{22}\text{Ne}(\alpha,\text{n})^{25}\text{Mg}$  reaction - noteworthy only in stars with low metallicity - leads to a small neutron burst [CSG<sup>+</sup>09]. The pocket mass itself is a uniform mixture of carbon (20 – 25%), helium (73 – 78%) and the product of the  $^{13}\text{C}(\alpha,\text{n})$  reaction, namely  $^{16}\text{O}$  [BS88].

Based on this scenario, the physical conditions we will adopt for our calculations mainly refer to the C pocket physical site. It consists mainly of helium and carbon, to a minor extend also of oxygen. The few protons and heavier elements that were mixed down from the convective



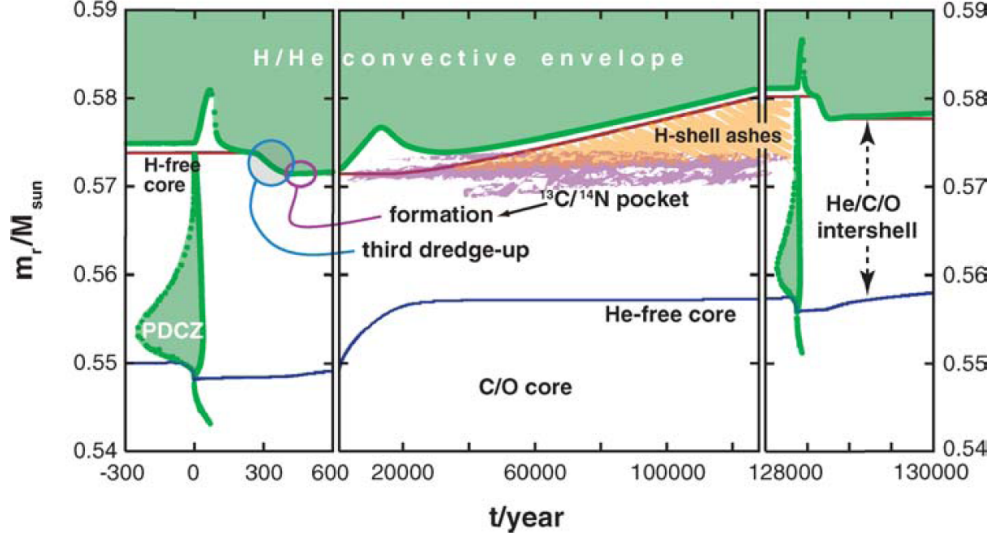


**Figure 2.5:** Schematic illustration of the mass region during the time  $t$  of two thermal pulses and their interpulse phase for a low-mass TP-AGB star (more precisely pulses 14 and 15 of a  $2 M_{\odot}$  star with metallicity 0.01), reproduced from [Her05]. PDCZ stands for pulse-driven convection zones and symbolizes the thermal pulses. The blue line tags the end of the CO core mass, the red one the end of the He containing shells, the dotted green one the boundaries of convection and the light green areas the convection zones. Note the varying timescales and the setting  $t = 0$  for the first considered pulse.

envelope in the third dredge-up as well as the s-process products that were already formed will be neglected as their abundance is barely noticeable compared to the major components. Two other constellations are chosen as well to compare the results with those already existing in the literature (see [TY83]). Our chosen plasma constituent parameters are

- a) 78% He, 20% C, 2%O,
- b) 73% He, 25% C, 2%O,
- c) 100% He,
- d) 75% H, 25% He.

The temperatures we select from  $T \sim 0.9 \cdot 10^8$  K to  $T \sim 3 \cdot 10^8$  K for the same reasons. Additionally we include a temperature of  $T = 3.48 \cdot 10^8$  K ( $\hat{=} \kappa T = 30\text{keV}$ ), because this is the lowest temperature considered in Ref. [Hel11] and was widely used in the literature to describe the s-process conditions according to the classical s-process model (see for example [Tak98]). For these parameters we can proceed to determine the ionization states of osmium with the help of the Saha equation.

### 3 Degree of Ionization in the Plasma

Since we are considering osmium in a hot and dense environment, where the slow (s-process) nucleosynthesis is taking place, it is indicated to assume the existence of ionized atoms in (approximate) thermodynamic equilibrium. The latter is due to a constant high temperature and density with increased collision rates [Ols61] over a long period of time. Though “chemical” reactions occur, the overall equilibrium concentrations of the reactants remain constant due to the principle of detailed balance, that states that every detailed process is statistically balanced by its precise reciprocal process [CG68]. Under these conditions the ratio of two neighboring ionization stages of a certain atom is described via the Saha-equation, named after Meghnad Saha, an Indian astrophysicist, who developed the equation in 1920 [Sah20] starting from thermodynamic considerations. The Saha equation has the form

$$\frac{n_{i,j+1}}{n_{i,j}} = \frac{b_{i,j+1}}{b_{i,j}} \cdot \left( \frac{m_{i,j+1}}{m_{i,j}} \right)^{\frac{3}{2}} \cdot \exp \left( -\frac{\chi_{i,j}}{\kappa T} - \eta \right), \quad (3.1)$$

with  $i$  being the atom species,  $j$  its ionization state,  $n_{i,j}$  the ion number density,  $b_{i,j}$  the partition function,  $m_{i,j}$  the ion mass,  $\chi_{i,j}$  the corrected ionization potential,  $\eta$  the degeneracy parameter,  $\kappa$  the Boltzmann’s constant and  $T$  the temperature [TY83].

In the following, we sketch the derivation of the above equation pursuing the approach presented in [CG68].

#### 3.1 Derivation of the Saha Equation

We assume thermodynamic equilibrium which includes thermal and chemical equilibrium. For thermal equilibrium the temperature has to stay constant in time within the considered space. While the chemical potential  $\mu$  can be described as the tendency of substances to change their location, chemical composition or state of aggregation [JH06] the chemical equilibrium refers to a situation where the driving forces compensate for each other. Every reaction will therefore proceed with the same rate as its reverse reaction. Applied to the ionization state  $j$  of the atom  $i$ , this leads to the equilibrium condition for the process of ionization

$$\mu_{ij} = \mu_{ij+1} + \mu_e, \quad (3.2)$$

with the subscript e denoting the electron. The chemical potential can be expressed through the energy  $E$  or the Gibbs energy  $G$  via

$$\mu_{ij} = \left. \frac{\partial E}{\partial N_{ij}} \right|_{S,V} = \left. \frac{\partial G}{\partial N_{ij}} \right|_{T,P}, \quad (3.3)$$

where  $N_{ij}$  describes the number of particles of the species  $i$  and ionization  $j$ ,  $S$  the entropy and  $V$  the volume. Statistical mechanics delivers with

$$f(E) = \frac{1}{\exp \left[ \frac{E-\mu}{\kappa T} \right] + 1} \quad (3.4)$$

a distribution function for an ideal gas obeying Fermi statistics via the negative derivative of the thermodynamic potential with respect to the chemical potential  $\mu$ . The thermodynamic

potential can be deduced from the Gibbs distribution for a variable number of particles (grand canonical ensemble) [LLP80]. The Bose-Einstein distribution that describes a system of bosons is similar to (3.4), but instead of the plus in the denominator a minus sign has to be applied.

To obtain the number  $dN$  of elements (fermions or bosons) in thermodynamic equilibrium having total energies per element between  $E$  and  $dE$ ,

$$dN = \frac{db}{\exp\left[\frac{E-\mu}{\kappa T}\right] \pm 1}, \quad (3.5)$$

we need not only the distribution function  $f(E)$ , but also the number of possible quantum states  $db$  corresponding to the energy range  $dE$  [LLP80, CG68]. Within a discrete energy level the statistical weight becomes equal to the degree of degeneracy  $b_i$ , which in the case of an electron with spin  $s = \frac{1}{2}$  is

$$b_i = b_e = 2s + 1 = 2. \quad (3.6)$$

For continuous energy levels, i.e., free particles, we follow the model used by Cox and Giuli [CG68] and constrain the space around the particle to a box of volume  $L^3$ . The de Broglie wavelength of the particle is

$$\lambda = \frac{h}{p}, \quad (3.7)$$

where  $h$  is the Planck constant and  $p$  the momentum of the particle. The periodic boundary conditions require for the one-dimensional case that

$$L = n_{x,y,z} \cdot \lambda_{x,y,z}, \quad n_{x,y,z} = 1, 2, \dots \quad (3.8)$$

for every direction  $(x, y, z)$ , so that

$$p_{x,y,z} = n_{x,y,z} \cdot \frac{h}{L}, \quad n_{x,y,z} = \pm 1, \pm 2, \dots \quad (3.9)$$

From equation (3.9) we get for a box in momentum space the volume

$$p_x p_y p_z = n_x n_y n_z \frac{h^3}{L^3} \quad (3.10)$$

containing the quantity of  $N_{\text{box}}$  quantum states, respectively nodes of the standing waves according to the boundary conditions,

$$N_{\text{box}} = (n_x + 1)(n_y + 1)(n_z + 1). \quad (3.11)$$

Our box in momentum space is assumed to be extremely large (meaning the values  $n_{x,y,z}$  are large), so that the expansion of our model into space holds for the free particle. Therefore we can approximate the number of quantum states per unit volume with the quotient of (3.11) and (3.10) as follows:

$$\left(1 + \frac{1}{n_x}\right) \left(1 + \frac{1}{n_y}\right) \left(1 + \frac{1}{n_z}\right) \frac{L^3}{h^3} \approx \frac{L^3}{h^3}. \quad (3.12)$$

This gives us a volume of  $h^3$  (called unit cell) per particle in phase space. If we now consider the phase space volume  $V \cdot p^2 dp \cdot d\Omega$  (confined to the solid angle  $d\Omega$  and to particles with momenta between  $p$  and  $dp$ ) the statistical weight of a free particle within this volume, meaning the number of unit cells it can occupy, can be described by

$$db = \frac{4\pi p^2 dp}{h^3} V. \quad (3.13)$$

According to the Pauli's principle, electrons can occupy the same quantum state twice, if they have different spins. Therefore equation (3.13) has to be multiplied by  $b_e$  in this case [FMT49]. With this knowledge we can determine the number density (number per volume) of electrons with energy  $E_e$  from (3.5):

$$n_e = \frac{N}{V} = \int_0^\infty b_e \frac{db}{V} f(E) = 2 \int_0^\infty \frac{4\pi p^2 dp}{h^3} \frac{1}{\exp\left[\frac{E_e - \mu}{\kappa T}\right] + 1}. \quad (3.14)$$

Most stable substances have a negative chemical potential; their resistance to react decreases with decreasing pressure and with increasing temperature [JH06]. We now focus on non-degenerate particles, corresponding to the constraint  $-\left(\frac{\mu}{\kappa T}\right) \gg 1$  (atoms or ions), of a certain charge state, corresponding to a specific ionization stage and in a discrete state  $k$  [CG68]. Then equation (3.5) reduces to the Maxwell-Boltzmann distribution

$$N_k = b_k e^{\mu/(\kappa T)} e^{-\epsilon_k/(\kappa T)}, \quad (3.15)$$

where  $\epsilon_k$  is the excitation potential. The ratio of two excitation levels  $k$  and  $o$  delivers the so-called *Boltzmann equation*:

$$\frac{N_k}{N_o} = \frac{b_k}{b_o} e^{-\epsilon_{ko}/(\kappa T)}, \quad \epsilon_{ko} = \epsilon_k - \epsilon_o. \quad (3.16)$$

We are interested in the ionization states. If an atom of species  $i$  in ionization state  $j$  and excitation state  $k$  (we call this particle 1) is further ionized, the resulting products are a free electron and the atom in ionization and excitation states  $j+1$  and  $o$  (in the following denoted as particle 2). For the atoms and ions (not for the electrons) we assume non-relativistic behavior due to their higher mass. The corresponding energies are

$$\text{particle 1} : \quad E_{i,j,k} = \frac{p_1^2}{2m_{i,j}} + \epsilon_{i,j,k}, \quad (3.17)$$

$$\text{particle 2} : \quad E_{i,j+1,o} = \frac{p_2^2}{2m_{i,j+1}} + \epsilon_{i,j+1,o} + I_{i,j} - m_e c^2, \quad (3.18)$$

$$\text{electron} : \quad E_e. \quad (3.19)$$

In the expression above,  $m$  is the particle mass and  $I_{i,j}$  denotes the ionization potential, i.e., the minimum energy required to remove an electron from the ground state of the  $j$ -times ionized atom [VGK94, Bra08]. In a slight change to the explanation of Cox and Giuli [CG68] we treat the electrons relativistically. Since the ionization potentials only involve the binding energies not the mass loss of the atom, the rest energy of the electron needs to be subtracted from the energy of particle 2. Consequently  $E_e$  contains the kinetic and the rest energy of the electron.

If we want to evaluate the number density for the particles 1 and 2 we need to know their number of possibly occupied quantum states. Those we can derive from the sum over the statistical weights per excitation level times the weighting factor and therefore are given by the partition function [LLP80]

$$b_{i,j} = \sum_k b_{i,j,k} \exp\left(-\frac{\epsilon_{i,j,k}}{\kappa T}\right). \quad (3.20)$$

Together with the approximation of (3.5) for  $-\left(\frac{\mu}{\kappa T}\right) \gg 1$  and the condition for chemical equilibrium (3.2) we obtain the following number densities:

$$\text{particle 1} : \quad n_{i,j} = b_{i,j} e^{\frac{\mu_{i,j+1} + \mu_e}{\kappa T}} \int_0^\infty \frac{4\pi p^2 dp}{h^3} e^{-\frac{p^2}{2m_{i,j}\kappa T}}, \quad (3.21)$$

$$\text{particle 2} : \quad n_{i,j+1} = b_{i,j+1} e^{-\frac{I_{i,j}}{\kappa T}} e^{\frac{m_e c^2}{\kappa T}} e^{\frac{\mu_{i,j+1}}{\kappa T}} \int_0^\infty \frac{4\pi p^2 dp}{h^3} e^{-\frac{p^2}{2m_{i,j+1}\kappa T}}. \quad (3.22)$$

The integration results in

$$n_{i,j} = b_{i,j} e^{\frac{\mu_{i,j+1}}{\kappa T}} e^{\frac{\mu_e}{\kappa T}} \frac{(2\pi m_{i,j}\kappa T)^{3/2}}{h^3}, \quad (3.23)$$

$$n_{i,j+1} = b_{i,j+1} e^{-\frac{I_{i,j}}{\kappa T}} e^{\frac{m_e c^2}{\kappa T}} e^{\frac{\mu_{i,j+1}}{\kappa T}} \frac{(2\pi m_{i,j+1}\kappa T)^{3/2}}{h^3}. \quad (3.24)$$

Now we only need to divide  $n_{i,j+1}$  by  $n_{i,j}$  to obtain the Saha-equation:

$$\frac{n_{i,j+1}}{n_{i,j}} = \frac{b_{i,j+1}}{b_{i,j}} \left( \frac{m_{i,j+1}}{m_{i,j}} \right)^{3/2} \exp \left( -\frac{I_{i,j}}{\kappa T} + \frac{m_e c^2}{\kappa T} - \frac{\mu_e}{\kappa T} \right). \quad (3.25)$$

## 3.2 Chemical Potential

So far the chemical potential is unknown. It is related to the energy of a particle through (3.3). In the following we ascribe the negative rest mass of the electron to the chemical potential and define the degeneracy parameter included in (3.1) according to [TY83] as

$$\eta = \frac{\mu_e - m_e c^2}{\kappa T}. \quad (3.26)$$

Consequently the electron number density (3.14) needed to obtain the chemical potential (thus the degeneracy parameter) changes its appearance. As  $E_e = \sqrt{m_e^2 c^4 + p^2 c^2}$  is the relativistic energy of the electron we make the notations

$$w := \sqrt{1 + \frac{p^2}{m_e^2 c^2}} \quad \text{and} \quad \beta := \frac{m_e c^2}{\kappa T}, \quad (3.27)$$

so that  $\frac{E_e}{\kappa T} = \beta w$ ,  $p = m_e c \sqrt{w^2 - 1}$  and  $\frac{dp}{dw} = \frac{m_e c w}{\sqrt{w^2 - 1}}$ . Equation (3.14) then transforms into

$$n_e = \frac{8\pi m_e^3 c^3}{h^3} \int_1^\infty \frac{w \sqrt{w^2 - 1}}{\exp(\beta w - \frac{\mu_e}{\kappa T})} dw = \frac{8\pi m_e^3 c^3}{h^3} \int_1^\infty \frac{w \sqrt{w^2 - 1}}{\exp(\beta(w - 1) - \eta)} dw. \quad (3.28)$$

In our consideration,  $n_e$  identifies the number density not only of the electrons resulting from the ionization of osmium, but also of the other plasma electrons. Actually the latter are the only ones of interest, because in all considered cases osmium can be treated as a tiny remainder whose ionization has no impact on the plasma composition. The plasma composition itself is determined by lighter elements.

Since both  $n_e$  and  $\eta$  are unknown, we use the charge neutrality of the plasma to get another expression for  $n_e$ . For every ion with a certain charge number, the corresponding same number of electrons are also present in the plasma. All we need to know are the number densities  $n_{i,j}$  of the ions in the plasma. From the given total mass density  $\rho$  and the individual mass fractions

$x_i$  we can obtain the atom number densities  $n_{i,j}$ , if we know the masses  $m_{i,j}$  and the respective ionization states:

$$\sum_j m_{i,j} n_{i,j} = \rho x_i. \quad (3.29)$$

We then can assign the charge numbers to the ion densities and calculate the electron number density via

$$n_e = \rho \sum_i x_i \left( \frac{\sum_j j n_{i,j}}{\sum_j m_{i,j} n_{i,j}} \right) = \sum_{i,j} j n_{i,j}. \quad (3.30)$$

Whereas the ion masses can safely be approximated by those of the respective neutral atoms, the ionization states can only be extracted by combining the calculation of the degeneracy parameter  $\eta$  with the evaluation of the Saha-equation in a self-consistent way [TY83]. Practically one chooses an initial ionization distribution to compute  $n_e$  from (3.30). This result is used to calculate a first value for  $\eta$  with (3.28) which applied to the Saha-equation delivers a new ionization distribution for equation (3.30). Now the whole process is repeated iteratively until the values converge and  $\eta$  has a definite value.

### 3.3 Continuum Depression

The electrons of the plasma not only deliver the degeneracy parameter  $\eta$ , their distribution also influences the binding energies of the ions in the plasma via screening effects. These lead to a diminished Coulomb-interaction between the nucleus and its bound electrons corresponding to reduced binding energies. In addition, the electrostatic potentials of neighboring ions in the plasma also lead to a reduction of the binding energies. Combined with the resonance broadening of atomic states into energy-bands due to the overlap of electron wave functions on adjacent atoms, these effects are even able to break the binding of outer electrons, a process called pressure ionization [Mor82]. The reduction of the binding energies is also called depression of the continuum, since it enables the bound electrons to reach the continuum with less energy input. This continuum depression affects the Saha-equation in two respects: on the one hand it results in the lowering of the measured or calculated vacuum ionization potential  $I_{i,j}$ . On the other hand it delivers a cut-off value for the summation within the partition function  $b_{i,j}$  (3.20). An isolated atom or ion has infinitely many excited levels, whose energies do not exceed the ionization potential [VGK94]. If this atom is surrounded by other charged particles, the corresponding continuum lowering counteracts the divergence, since highly excited levels whose energies correspond to or exceed the lowered ionization potential are treated as unoccupied in favor of the next ionization state [CG68]. Again the ion distribution of the plasma is required for the determination of the continuum depression and the other way around, which demands for a self-consistent solution.

To calculate the continuum depression we basically follow the finite-temperature Thomas-Fermi model extended by Steward and Pyatt to include neighboring ions, valid for non-degenerate and non-relativistic electrons [SPJ66]. In a first step, we outline the non-relativistic treatment, followed, in a second step, by the extension of the model to account for relativistic electrons, which is our case of interest. In both steps we also introduce a correction to account for the quantum mechanical behavior of the bound electrons.

### 3.3.1 Non-Relativistic Case

Our first aim is to obtain the electrostatic potential of the nucleus. To this end we need to solve the Poisson equation with the help of the charge distribution of the plasma including the bound electrons of the respective ion. The nature of the distribution is such that the Poisson equation can only be solved numerically. To avoid overly long calculation periods we will find analytical approximations for the charge distribution in the extremal regions close to and far away from the nucleus. The middle part we keep computing numerically. In the direct proximity of the nucleus we also modify the charge distribution by adopting a quantum mechanical treatment. With the resulting potential of the nucleus we then find an expression for the charge distribution of the plasma particles only. This time the bound electrons of our ion are excluded. By solving the Poisson equation of this distribution we finally obtain the perturbing potential, that delivers us the desired continuum depression.

Before we proceed, a few additional assumptions should be made. We consider a point-like nucleus with positive charge  $Ze$ ,  $e$  being the absolute value of the electron charge, in a homogeneous and time-averaged environment consisting of point-like ions and electrons, all at a fixed temperature  $T$ .

#### 3.3.1.1 Formal Derivation of the Nuclear Potential

Since the charge density is supposed to be spherically symmetric around the nucleus, its electrostatic potential  $\Phi$  can be determined via the Poisson equation as follows [SPJ66, TY83]:

$$\begin{aligned}\Delta\Phi(\vec{r}) &= \frac{1}{r^2} \frac{\partial}{\partial r} \left( r^2 \frac{\partial\Phi(r)}{\partial r} \right) = \left( \frac{2}{r} \frac{\partial}{\partial r} + \frac{\partial^2}{\partial r^2} \right) \Phi(r) \\ &= \frac{1}{r} \frac{\partial^2}{\partial r^2} (r\Phi(r)) = -4\pi e \left( \sum_{i,j} j n_{i,j}(r) - n_e(r) \right).\end{aligned}\quad (3.31)$$

Here,  $n_e(r)$  and  $n_{i,j}(r)$  give the local electron and ion number densities as functions of the radial distance  $r$  from the nucleus due to its potential  $\Phi(r)$  in contrast to the expressions (3.23) and (3.14). The latter, denoted as  $n_e(\infty)$  and  $n_{i,j}(\infty)$ , will be valid as asymptotic densities as  $r$  approaches infinity, for we can assume the electrostatic potential of the nucleus to vanish at infinity in the supposedly neutral plasma. To obtain the equations for  $n_e(r)$  and  $n_{i,j}(r)$  the potential energy  $e\Phi(r)$  has to be included in the equations (3.17) and (3.19). Thus, we obtain an additional factor of  $e^{-\frac{j e \Phi(r)}{\kappa T}}$  in  $n_{i,j}(r)$ , resulting in

$$n_{i,j}(r) = n_{i,j}(\infty) \frac{n_{i,j}(r)}{n_{i,j}(\infty)} = n_{i,j}(\infty) \cdot e^{-\frac{j e \Phi(r)}{\kappa T}}. \quad (3.32)$$

The treatment of  $n_e(r)$  is slightly more complicated because we stick to the Fermi-Dirac statistics, distribution (3.4). For non-relativistic energies it is also useful to rewrite equation (3.14) by substituting  $\frac{p^2}{2m_e \kappa T}$  for  $z$  and  $\frac{p}{m_e \kappa T} dp$  for  $dz$ :

$$n_e(\infty) = \frac{4\pi(2m_e \kappa T)^{3/2}}{h^3} \int_0^\infty \frac{\sqrt{z}}{\exp(z - \frac{\mu_e}{\kappa T}) + 1} dz = \frac{4\pi(2m_e \kappa T)^{3/2}}{h^3} F_{nr} \left( \frac{\mu_e}{\kappa T} \right). \quad (3.33)$$

Here we introduce the Fermi-Dirac integral [MVR95]

$$F_{nr}(t) = \int_0^\infty \frac{\sqrt{z}}{\exp(z - t) + 1} dz. \quad (3.34)$$

In this manner  $n_e(r)$  can be expressed as

$$n_e(r) = \frac{4\pi(2m_e\kappa T)^{3/2}}{h^3} F_{nr} \left( \frac{e\Phi(r) + \mu_e}{\kappa T} \right) = n_e(\infty) \frac{F_{nr}((e\Phi(r) + \mu_e)/(\kappa T))}{F_{nr}(\mu_e/(\kappa T))} \quad (3.35)$$

in accordance with Steward and Pyatt [SPJ66]. Taking into account the neutrality of the plasma, which according to (3.30) results in the assumption

$$\sum_{i,j} j n_{i,j}(\infty) = n_e(\infty) \quad (3.36)$$

and delivers through it the value  $\mu_e/(\kappa T)$ , the Poisson equation (3.31) assumes the shape

$$\frac{1}{r} \frac{\partial^2}{\partial r^2} (r\Phi(r)) = -4\pi e \sum_{i,j} \left( e^{-\frac{j e\Phi(r)}{\kappa T}} j n_{i,j}(\infty) - \frac{F_{nr}((e\Phi(r) + \mu_e)/(\kappa T))}{F_{nr}(\mu_e/(\kappa T))} j n_{i,j}(\infty) \right). \quad (3.37)$$

To obtain a more compact version of this equation it is reasonable to introduce the dimensionless quantities [SPJ66]

$$y = \frac{e\Phi}{\kappa T}, \quad x = \frac{r}{D}, \quad (3.38)$$

with the Debye-length

$$D = \frac{1}{\sqrt{(4\pi e^2/\kappa T) \sum_{i,j} (j^2 + j) n_{i,j}(\infty)}}. \quad (3.39)$$

The left hand side of equation (3.37) transforms as follows:

$$\frac{1}{r} \frac{\partial^2}{\partial r^2} (r\Phi(r)) = \frac{1}{D^2} \frac{\kappa T}{e} \frac{1}{x} \frac{\partial^2}{\partial x^2} (xy) = 4\pi e \sum_{i,j} (j+1) j n_{i,j}(\infty) \frac{1}{x} \frac{\partial^2}{\partial x^2} (xy). \quad (3.40)$$

We equate with the right hand side of (3.37) to get

$$\begin{aligned} \frac{1}{x} \frac{\partial^2}{\partial x^2} (xy) &= \frac{\sum_{i,j} j n_{i,j}(\infty) \left( \frac{F_{nr}(y + \mu_e/(\kappa T))}{F_{nr}(\mu_e/(\kappa T))} - e^{-jy} \right)}{\sum_{i,j} j n_{i,j}(\infty) (j+1)} \\ &= \frac{F_{nr}(y + \mu_e/(\kappa T))}{I_{1/2}(\mu_e/(\kappa T))} \frac{\sum_{i,j} j n_{i,j}(\infty)}{\sum_{i,j} j n_{i,j}(\infty) (j+1)} - \frac{\sum_{i,j} j n_{i,j}(\infty) e^{-jy}}{\sum_{i,j} j n_{i,j}(\infty) (j+1)} \\ &= \frac{F_{nr}(y + \mu_e/(\kappa T))}{F_{nr}(\mu_e/(\kappa T))} \frac{\sum_{i,j} j n_{i,j}(\infty)}{\sum_{i,j} j n_{i,j}(\infty) (j+1)} - \frac{\sum_{i,j} e^{-jy} j n_{i,j}(\infty)}{\sum_{i,j} j n_{i,j}(\infty)} \frac{\sum_{i,j} j n_{i,j}(\infty)}{\sum_{i,j} j n_{i,j}(\infty) (j+1)} \\ &= \frac{F_{nr}(y + \mu_e/(\kappa T))}{F_{nr}(\mu_e/(\kappa T))} \frac{1}{\langle j+1 \rangle} - \frac{\langle e^{-jy} \rangle}{\langle j+1 \rangle}. \end{aligned} \quad (3.41)$$

In the last step we have introduced average values weighted with  $j n_{i,j}(\infty)$  [TY83],

$$\langle X \rangle = \frac{\sum_{i,j} X j n_{i,j}(\infty)}{\sum_{i,j} j n_{i,j}(\infty)}. \quad (3.42)$$

With the definitions  $j^* := \langle j \rangle = \langle j+1 \rangle - 1$  and

$$Y(x) := xy, \quad a := \frac{\mu_e}{\kappa T} \quad (3.43)$$



we finally need to solve the Poisson equation of the form

$$\frac{d^2}{dx^2}Y(x) = \frac{x}{1+j^*} \left[ \frac{F_{nr}(Y(x)/x+a)}{F_{nr}(a)} - \langle e^{-jY(x)/x} \rangle \right] \quad (3.44)$$

to derive the potential of the nucleus  $\Phi$  through  $Y(x)$ . Since  $\Phi(r) \rightarrow 0$  for  $r \rightarrow \infty$  and  $\Phi(r) \rightarrow \frac{Ze}{r}$  for  $r \rightarrow 0$ , the boundary conditions for  $Y$  are  $Y(x) \rightarrow 0$  for  $x \rightarrow \infty$  and  $Y(x) = yx = \frac{e\Phi}{\kappa T} \frac{r}{D} \rightarrow \frac{Ze^2}{\kappa T} =: Y_0$  for  $x \rightarrow 0$ .

In order to solve (3.44) efficiently, we split the charge distribution on the right hand side in three parts, corresponding to the regions close to the nucleus, far away from the nucleus and in between. In the central region the distribution has a regular appearance, such that we can treat the problem numerically. The region close to the nucleus is where the nuclear potential reaches high values, which suggests an asymptotic analytical treatment to avoid numerical defects. At the other end, since the charge distribution shows a steep behavior in the part that corresponds to the region far from the nucleus, we again introduce an approximation. Following this treatment, we proceed to include a quantum mechanical correction of the charge distribution in order to solve the Poisson equation.

The approximations used in the next subsections are valid for  $\exp(-\frac{\mu_e}{\kappa T}) \gg 1$  and non-degenerate free electrons.

### 3.3.1.2 Expansion Close to the Nucleus

An efficient way to approach the solution of (3.44) numerically is to expand the quotient of the two Fermi-Dirac integrals. With at least a partial analytical construction of the Poisson equation (3.44) the computing time can significantly be reduced. We consider here the region close to the nucleus, where the Coulomb potential increases rapidly. Under the assumption  $Y/x = y \gg -a$  we get [SPJ66]

$$\frac{F_{nr}(Y(x)/x+a)}{F_{nr}(a)} \approx \frac{4}{3\sqrt{\pi}} e^{-a} \left( \frac{Y(x)}{x} + a \right)^{3/2} \left[ 1 + \frac{\pi^2}{8(\frac{Y(x)}{x} + a)^2} \right]. \quad (3.45)$$

A numerical check confirms the good agreement of both sides of the above equation for high enough  $Y(x)/x$ -values. In this regime the approximation can be safely applied.

For  $y \gg -a$  the Poisson equation converges to the zero-temperature Thomas-Fermi equation where the density of the bound electrons and those of the free electrons converge as  $x^{-3/2}$  and  $x^{-1/2}$ , respectively [SPJ66]. This implies for  $y(x)$ ,

$$y(x) = \frac{Y_0}{x} + s + \mathcal{O}(x^{1/2}), \quad (3.46)$$

$$Y(x) = Y_0 + sx + \mathcal{O}(x^{3/2}), \quad (3.47)$$

where the constant of the first term  $Y_0$  is given through the boundary condition and  $s$  is another constant value. The latter is given by the derivative of  $Y$  in the point where this approximation branch merges the numerically computed values of  $Y$  corresponding to the central branch. We choose this point sufficiently close to the nucleus, e.g.,  $x = 10^{-4}$ . Later we can control our choice by plugging this value into the derived solution of the Poisson equation divided by  $x$ ,  $Y(x)/x = y$ . The result we set into the right hand side of the Poisson equation (3.44), once by using the fraction of the Fermi integrals, once by using (3.45). The difference should be conveniently small (e.g.  $\leq 1\%$ ).

### 3.3.1.3 Expansion Far From the Nucleus

In the other extreme, at  $Y/x = y \ll -a$  (where the nuclear potential is small), following Stewart and Pyatt [SPJ66] the expansion reads

$$\frac{F_{nr}(Y(x)/x + a)}{F_{nr}(a)} \approx e^{Y(x)/x} \left[ 1 - 2^{-3/2} e^{Y(x)/x+a} (1 - e^{-Y(x)/x}) \right]. \quad (3.48)$$

According to [SPJ66] the right hand side of equation (3.44) will then become equal to  $xy = Y$ . In fact we can show that the Poisson equation (3.44) approaches  $Y$  for the considered small  $y$ , starting with a Taylor expansion of  $F_{nr}(Y(x)/x + a) = F_{nr}(y + a)$  and keeping only the first two terms at  $y = 0$ :

$$\begin{aligned} F_{nr}(y + a) &\approx \int_0^\infty \frac{t^{1/2} dt}{\exp(t - a - y) + 1} \\ &\approx F_{nr}(a) + \left. \frac{dF_{nr}(y + a)}{dy} \right|_{y=0} \cdot y \\ &= F_{nr}(a) + \int_0^\infty t^{1/2} dt \left. \frac{d}{dy} \frac{1}{\exp(t - a - y) + 1} \right|_{y=0} \cdot y \\ &= F_{nr}(a) + \int_0^\infty \frac{\exp(t - a - y) t^{1/2} dt}{(\exp(t - a - y) + 1)^2} \Big|_{y=0} \cdot y \\ &= F_{nr}(a) + \left( \int_0^\infty \frac{(\exp(t - a) + 1) t^{1/2} dt}{(\exp(t - a) + 1)^2} - \int_0^\infty \frac{t^{1/2} dt}{(\exp(t - a) + 1)^2} \right) \cdot y \\ &= F_{nr}(a) + y F_{nr}(a) - y \int_0^\infty \frac{t^{1/2} dt}{(\exp(t - a) + 1)^2}. \end{aligned} \quad (3.49)$$

The last integral in (3.49) amounts to maximally 0.005 for all  $a < -2$  and vanishes very fast for smaller  $a$ . It will therefore be neglected. Instead of the term  $\langle e^{-jy} \rangle$  of equation (3.44) we can use the approximation  $e^{-\langle j \rangle y}$ , which we expand further, since  $y \ll -a$ :

$$e^{-\langle j \rangle y} = e^{-j^* y} \approx 1 - j^* y. \quad (3.50)$$

Therefore, the Poisson equation behaves as

$$\frac{d^2}{dx^2} Y(x) \approx \frac{x}{1 + j^*} \left[ \frac{F_{nr}(a) + Y(x)/x F_{nr}(a)}{F_{nr}(a)} - (1 - j^* Y(x)/x) \right] = \frac{x}{1 + j^*} Y(x)/x (1 + j^*) = Y. \quad (3.51)$$

Numerical values again confirm this approach. As a solution for (3.51) we obtain

$$Y(x) = C e^{-x}, \quad (3.52)$$

$$y(x) = \frac{C}{x} e^{-x}, \quad (3.53)$$

with  $C$  a constant. For a fixed value  $x_{\text{fix}}$ ,  $C$  can be obtained from  $C = Y(x_{\text{fix}})/e^{-x_{\text{fix}}}$ .  $Y(x_{\text{fix}})$  on the other hand is derived from the numerical solution of the central part of the Poisson equation. For  $x_{\text{fix}}$  we take the chosen threshold value, where we start applying this approximation instead of the numerically calculated values. On such a threshold the values from both methods have to agree up to the second derivative. We control the validity of  $x_{\text{fix}}$  later (when we derived the final function  $Y(x)$ ) by solving  $Y(x_{\text{fix}})/x_{\text{fix}}$  and checking if the assumption (3.51) holds for this value.

### 3.3.1.4 Quantum Mechanical Corrections

Instead of mere simplifying the Fermi model, it might be more useful to investigate its validity in the region close to the nucleus in general. A not fully ionized ion has an electron shell structure, whereas the Fermi-model based on the continuously acting potential of the nucleus implies a continuous electron distribution as well as locally free electrons. Furthermore, according to the infinite potential at the origin, the model electron density and with it the kinetic-energy density is supposed to become infinite, as apparent from equation (3.46). This is obviously not true and contradicts what we know from quantum mechanics: the electron density is constant and the kinetic-energy density zero at the nucleus [AH70]. By far the biggest contribution to the electron density there ( $> 87.5\%$ ) originates from the K-shell electrons [AH70]. Since we know the Coulomb form of the nuclear potential, we can apply the corresponding solution of the Schrödinger equation, use the Hartree approximation for the K-shell wave functions and finally get an approximate exponential density in the nuclear region [AH70],

$$n_e(r) \approx \frac{\tilde{A}}{n_e(\infty)} e^{-\tilde{B}r} n_e(\infty), \quad r < r_0. \quad (3.54)$$

The point  $r_0$  has yet to be determined in a self-consistent way as well as the constants  $\tilde{A}$  and  $\tilde{B}$ . To apply this exponential number density form to our Poisson equation (3.44), we use the dimensionless parameters (3.38) once again. This—together with the divisor  $n_e(\infty)$ —only transforms the yet unknown constants  $\frac{\tilde{A}}{n_e(\infty)} \rightarrow A$ ,  $\tilde{B} \rightarrow B$ ,  $r_0 \rightarrow x_0$ .

Thus the Poisson equation takes the form

$$\frac{d^2}{dx^2} Y_{qm}(x) = \frac{x}{1+j^*} \left[ A e^{-Bx} - \langle e^{-jY(x)/x} \rangle \right], \quad x < x_0. \quad (3.55)$$

Once again we need the numerical solution of the central Poisson equation (3.44), this time also with the included approximation for distances close to the nucleus, to derive the unknown constants from the merging point. In the following, we denote the combination of both branches as central or middle or numerical part of  $Y$ , leaving the region close to the nucleus to be handled quantum mechanically. The numerical solution  $Y(x)$  can be achieved with the help of the point  $x_{\text{fix}}$ , where the exponential approximation for large  $x$  merges. Since

$$\frac{d}{dx} Y(x)|_{x=x_{\text{fix}}} = \frac{d}{dx} (C e^{-x})|_{x=x_{\text{fix}}} = -C e^{-x_{\text{fix}}} = -Y(x_{\text{fix}}), \quad (3.56)$$

one boundary condition for (3.44) is the identity  $Y'(x_{\text{fix}}) = -Y(x_{\text{fix}})$ . The other will be the actual value of  $Y(x_{\text{fix}})$ . However, this parameter can only be obtained together with the adjustment of the other merging constraints at location  $x_0$ ,

$$Y_{qm}(x_0) = Y(x_0), \quad \frac{d}{dx} Y_{qm}(x)|_{x=x_0} = \frac{d}{dx} Y(x)|_{x=x_0}, \quad \frac{d^2}{dx^2} Y_{qm}(x)|_{x=x_0} = \frac{d^2}{dx^2} Y(x)|_{x=x_0}. \quad (3.57)$$

The solutions must therefore be again derived in a self-consistent way. For a start, the numerical solution  $Y(x)$  of the middle part—Poisson equation (3.44)—has to be treated as dependent also of this unknown value  $Y(x_{\text{fix}})$  and the solution  $Y_{qm}(x)$  for the Poisson equation (3.55) including quantum mechanical corrections as a function of  $x$  and  $x_0$  ( $Y_{qm}(x, x_0)$ ). This implies that  $A$  and  $B$  can be fixed except for their dependence on  $x_0$ . To get  $A$  and  $B$  we note that

$$A e^{-Bx_0} = \frac{F_{nr}(Y(x_0)/x_0 + a)}{F_{nr}(a)} \quad (3.58)$$

due to the match of (3.44) and (3.55) at  $x_0$ . The derivatives of the left hand side of (3.58) can be easily computed:

$$\frac{d}{dx} (A e^{-Bx}) = -B(A e^{-Bx}), \quad \frac{d^2}{dx^2} (A e^{-Bx}) = B^2(A e^{-Bx}). \quad (3.59)$$

Since at  $x_0$  we require a smooth function, the derivatives of  $Ae^{-Bx}$  can be replaced by those of  $F_{nr}(Y(x)/x+a)/F_{nr}(a)$  there. This enables us to calculate  $A$  and  $B$  as functions of  $x_0$ ,

$$B(x_0) = - \left( \frac{d}{dx} \frac{F_{nr}\left(\frac{Y(x)}{x} + a\right)}{F_{nr}(a)} \Big|_{x=x_0} \right) / \frac{F_{nr}(Y(x_0)/x_0 + a)}{F_{nr}(a)}, \quad (3.60)$$

$$A(x_0) = \frac{F_{nr}(Y(x_0)/x_0 + a)}{F_{nr}(a)} / e^{-Bx_0}, \quad (3.61)$$

and emphasizes the  $x_0$ -dependence of  $\frac{d^2}{dx^2}Y_{qm}(x)$ , (3.55).

Fortunately, we also know that the value  $Y_{qm}(0)$  of our quantum mechanical adjusted Poisson equation (3.55) has to be equal to  $Y_0$ . This additional information enables us to determine  $x_0$  via

$$Y_{qm}(0, x_0) = Y_0 \Rightarrow x_0 \Rightarrow Y_{qm}(x) \quad (3.62)$$

and fix  $A$  and  $B$ . With the value  $Y_{qm}(x_0) = Y(x_0)$  the determination of  $Y(x)$  and  $Y(x_{\text{fix}})$  can be completed.

Our considerations result in a distribution for the potential energy of the nucleus in units of  $\kappa T$ ,  $y(x)$ , that is split in three parts, smoothly merging in  $x_0$  and  $x_{\text{fix}}$ . If we denote the solution of (3.51) as  $Y_{\text{approx}}$  and the one of (3.44) together with (3.47) as  $Y_{\text{num}}$  we can formulate

$$y(x) = \begin{cases} Y_{qm}(x)/x & \text{for } x \leq x_0, \\ Y_{num}(x)/x & \text{for } x_0 \leq x \leq x_{\text{fix}}, \\ Y_{approx}(x)/x & \text{for } x_{\text{fix}} \leq x. \end{cases} \quad (3.63)$$

### 3.3.1.5 Perturbing Potential

So far we have considered only the potential of the nucleus we are mainly interested in (in our case osmium), in its plasma environment. Consequently we have included all electrons that surround the nucleus (plasma electrons and bound electrons of the respective ion), in describing the plasma. The bound electrons of the ion, however, cannot be attributed to the perturbing plasma. If we want to evaluate the effect of the perturbing potential  $\Phi_{\text{pert}}(r)$  of the plasma ions and plasma electrons on our ion, we therefore need an expression that excludes the bound electrons of the respective ion. In comparison to (3.35), the local electron distribution for the perturbing plasma, hence for the free electrons, is of the form

$$\begin{aligned} n_{e,\text{pert}}(r) &= \frac{4\pi(2m_e\kappa T)^{3/2}}{h^3} \int_y^\infty \frac{\sqrt{z}}{\exp(z - (\frac{\mu_e}{\kappa T} + y)) + 1} dz = \frac{4\pi(2m_e\kappa T)^{3/2}}{h^3} G_{nr}\left(\frac{\mu_e}{\kappa T} + y, y\right) \\ &= n_e(\infty) \frac{G_{nr}(\mu_e/(\kappa T) + y, y)}{F_{nr}(\mu_e/(\kappa T))} = n_e(\infty) \frac{G_{nr}(a + y, y)}{F_{nr}(a)}. \end{aligned} \quad (3.64)$$

The integration starts from  $y$ , because the kinetic energy of the electrons has to exceed the potential energy  $e\Phi$  for them to be free, leading to  $z > y$ . Correspondingly all electrons with energy smaller than  $e\Phi$  are assumed to be bound.

For the dimensionless form of the perturbing potential  $v := \frac{e\Phi_{\text{pert}}}{\kappa T}$  and with the same considerations as in section 3.3.1.1 we obtain the differential equation

$$\frac{1}{x} \frac{\partial^2}{\partial x^2}(xv) = \frac{1}{j^* + 1} \left[ \frac{G_{nr}(a + y, y)}{F_{nr}(a)} - \langle e^{-jy} \rangle \right] =: S(x) \quad (3.65)$$

with the boundary condition that  $v(x)$  is finite in the origin ( $r = 0$ ) and its derivative constant ( $\frac{\partial v(x)}{\partial x} = 0$ ) [SPJ66]. Furthermore, we require that the perturbing potential is zero at infinity. This causes  $v(x)$  to be negative everywhere else in contrast to the nuclear potential  $y$ , which increases with the smaller the distance to the nucleus (origin), where it diverges. The opposite behaviors of the two potentials becomes obvious through the signs.

It is noteworthy that  $S(x)$ , the right hand side of (3.65), does not contain the perturbing potential  $v(x)$  anymore, but only  $y(x)$ , that we can obtain from (3.63) and (3.43). Thus the evaluation of  $S(x)$  is already possible. The continuum depression can be regarded as the negative perturbing potential energy ( $e\Phi_{\text{pert}} = v\kappa T$ ) averaged over the ion orbital from which the electron is being removed ( $-\bar{v}\kappa T$ ) [SPJ66]. Except for highly excited orbitals, the substitution  $-\bar{v} \rightarrow -v(0)$  is reasonable, since the orbital's range is close to the nucleus. We also know that  $v(x)$  reaches a constant value at the origin, where its derivative is zero. Thus, the next step must be to extract  $v(0)$ . Using the general approach

$$\frac{d^2}{dx^2}(xv(x)) = \frac{d}{dx}(v(x) + xv'(x)) = v'(x) + v'(x) + xv''(x) = 2v'(x) + xv''(x), \quad (3.66)$$

the integration of equation (3.65) gives the expressions

$$\frac{d}{dx}(xv(x)) = \int_0^x d\tilde{x} \tilde{x} S(\tilde{x}) + v(0), \quad (3.67)$$

$$xv(x) = \int_0^x dt \int_0^t d\tilde{x} \tilde{x} S(\tilde{x}) + xv(0). \quad (3.68)$$

For iterated integrals over a smooth function  $f(x)$  the following rule [AS64] can be applied:

$$\int_0^x dt_n \int_0^{t_n} dt_{n-1} \dots \int_0^{t_3} dt_2 \int_0^{t_2} f(t_1) dt_1 = \frac{1}{(n-1)!} \int_0^x (x-t)^{n-1} f(t) dt. \quad (3.69)$$

Here,  $xS(x)$  is such a smooth function. Consequently the integral (3.68) transforms as

$$xv(x) = \int_0^x (x-t)tS(t)dt + xv(0) \quad (3.70)$$

leading to the expression

$$v(x) = v(0) + \frac{1}{x} \left( x \int_0^x tS(t)dt - \int_0^x tS(t)dt \right) = v(0) + \int_0^x tS(t)dt - \frac{1}{x} \int_0^x t^2 S(t)dt \quad (3.71)$$

for the perturbation. At infinite distance from the nucleus,  $v(x)$  vanishes due to the boundary conditions. The same is true for the last integral on the right hand side of equation (3.71) because of the factor  $x^{-1}$  as  $\int_0^x t^2 S(t)dt$  is assumed to be finite (see (3.76)). This enables us to calculate the perturbing potential energy in units of  $\kappa T$  directly via

$$v(0) = - \int_0^\infty tS(t)dt, \quad (3.72)$$

whereas the general form for  $v$  is

$$\begin{aligned}
 v(x) &= - \int_0^\infty tS(t)dt + \int_0^x tS(t)dt - \frac{1}{x} \int_0^x t^2 S(t)dt \\
 &= - \int_x^\infty tS(t)dt - \frac{1}{x} \int_0^x t^2 S(t)dt \\
 &= - \int_x^\infty tS(t)dt - \frac{1}{x} \int_0^\infty t^2 S(t)dt + \frac{1}{x} \int_x^\infty t^2 S(t)dt.
 \end{aligned} \tag{3.73}$$

For high values of  $x$ ,  $y(x)$  vanishes exponentially as well as the first and third integral on the last line in (3.73) due to the close boundaries. This delivers us the approximation

$$v(x) \rightarrow -\frac{1}{x} \int_0^\infty t^2 S(t)dt \quad \text{for } x \rightarrow \infty. \tag{3.74}$$

If we now want to consider only the nucleus with its bound electrons, but without the free plasma electrons and its ions, we know that only the effective Coulomb potential of the nucleus screened by its bound electrons will be noticed far from the nucleus [SPJ66, TY83]. Using dimensionless quantities, the respective expression is

$$y_{\text{screened}}(x) = y(x) - v(x) \approx 0 - \left( -\frac{1}{x} \int_0^\infty t^2 S(t)dt \right) = \frac{1}{x} \int_0^\infty t^2 S(t)dt, \tag{3.75}$$

giving the net ionic charge  $Z^*$  from

$$y_{\text{screened}}(x)x = \frac{e\Phi_{\text{screened}}}{\kappa T} \frac{r}{D} = \frac{Z^* e^2}{D\kappa T} = \int_0^\infty t^2 S(t)dt. \tag{3.76}$$

Moreover, given  $D$ ,  $T$  and  $Z^*$  together with the fixed value  $v(0)$ , the perturbation  $v(x)$  can be approximated. It turns out that only the ionic state  $j$  of the respective ion ( $= Z^*$ ) is of relevance, regardless of its atomic species  $i$  [TY83].

Finally, considering the threefold way to calculate the nuclear potential, the applied quantum mechanical corrections and the derivation of the perturbing potential as a function of the nuclear potential, we obtain the continuum depression energy  $\Delta_j$  as

$$\Delta_j = \kappa T \int_0^\infty tS(t)dt, \tag{3.77}$$

which implies the definition of the corrected ionization potential  $\chi_{i,j}$  from (3.1):

$$\chi_{i,j} = I_{i,j} - \Delta_j. \tag{3.78}$$

With this value for the continuum depression, we can calculate the partition functions and solve the Saha equation for the non-relativistic case. But before that, we first turn to the task of evaluating the relativistic continuum depression value.

### 3.3.2 Relativistic Calculation

After the description of the non-relativistic case, we proceed to include relativistic effects by considering the electrons as relativistic particles. All other assumptions applied in the non-relativistic case still hold.

#### 3.3.2.1 Formal Derivation of the Nuclear Potential

In the relativistic form,  $n_{e,r}(\infty)$  is consistent with (3.28),

$$n_{e,r}(\infty) = \frac{8\pi m_e^3 c^3}{h^3} \int_1^\infty \frac{w\sqrt{w^2-1}}{\exp(\beta(w-1)-\eta)} dw = \frac{8\pi m_e^3 c^3}{h^3} F_r(\eta), \quad (3.79)$$

where we have used the notation  $F_r$  for the relativistic Fermi-Dirac integral. Consequently, the local electron number density distribution through the additional energy  $e\Phi(r)$  reads

$$\begin{aligned} n_{e,r}(r) &= \frac{8\pi m_e^3 c^3}{h^3} \int_1^\infty \frac{w\sqrt{w^2-1}}{\exp(\beta(w-1)-\eta-\frac{e\Phi(r)}{\kappa T})} dw = \frac{8\pi m_e^3 c^3}{h^3} F_r\left(\eta + \frac{e\Phi(r)}{\kappa T}\right) \\ &= n_{e,r}(\infty) \frac{F_r(\eta + e\Phi(r)/(\kappa T))}{F_r(\eta)}. \end{aligned} \quad (3.80)$$

For the next steps the treatment is parallel to the non-relativistic one. With (3.38) and (3.43) we obtain the Poisson equation

$$\frac{d^2}{dx^2} Y_r(x) = \frac{x}{1+j^*} \left[ \frac{F_r(Y_r(x)/x + \eta)}{F_r(\eta)} - \langle e^{-jY_r(x)/x} \rangle \right], \quad (3.81)$$

for which the boundary conditions described in section 3.3.1.1, after equation (3.31), still hold.

As in the non-relativistic case we again split the charge density in three parts to account for its different behavior in every such region. Only the middle part we treat purely numerical. The parts close to and far from the nucleus we look at in the following with the aim to get analytically treatable asymptotics. Afterwards, quantum mechanical considerations are made.

#### 3.3.2.2 Expansion Close to the Nucleus

Following the procedure in the non-relativistic case, in order to save computational time we derive an asymptotic function for the charge distribution in the region close to the nucleus, meaning for large values of the nuclear potential. To simplify matters we define  $\alpha := y + \eta$  and expand

$$F_r(\alpha) = \int_1^\infty \frac{w\sqrt{w^2-1}}{\exp(\beta(w-1)-\alpha)+1} dw \quad (3.82)$$

for large  $\alpha$ . The distribution function of the Fermi gas  $(\exp(\beta(w-1)-\alpha)+1)^{-1}$  ranges between zero ( $w \gg w_0$ ) and one ( $w \ll w_0$ ). A sharp cutoff arises at

$$w_0 := \frac{\alpha}{\beta} + 1, \quad (3.83)$$

where the exponent of (3.82) becomes zero. Thus it is reasonable to split the integral  $F_r(\alpha)$  according to the different behavior on both sides of the cutoff,

$$F_r(\alpha) = \int_1^{w_0} \frac{w\sqrt{w^2-1}}{\exp(\beta(w-1)-\alpha)+1} dw + \int_{w_0}^{\infty} \frac{w\sqrt{w^2-1}}{\exp(\beta(w-1)-\alpha)+1} dw \quad (3.84)$$

$$= \int_1^{w_0} w\sqrt{w^2-1} dw - \int_1^{w_0} \frac{w\sqrt{w^2-1}}{\exp(\alpha-\beta(w-1))+1} dw + \int_{w_0}^{\infty} \frac{w\sqrt{w^2-1}}{\exp(\beta(w-1)-\alpha)+1} dw. \quad (3.85)$$

In the last step we have used the identity (see [LLP80])

$$\frac{1}{e^z + 1} = 1 - \frac{1}{e^{-z} + 1}. \quad (3.86)$$

Now we substitute as follows:

$$u := \alpha - \beta(w-1) \Rightarrow w = \frac{\alpha-u}{\beta} + 1, \quad \frac{du}{dw} = -\beta, \quad (3.87)$$

$$v := \beta(w-1) - \alpha \Rightarrow w = \frac{v+\alpha}{\beta} + 1, \quad \frac{dv}{dw} = \beta. \quad (3.88)$$

This transforms the second and third integral of (3.85), leading to

$$\begin{aligned} F_r(\alpha) = & \int_1^{w_0} w\sqrt{w^2-1} dw - \int_0^{\alpha} w\sqrt{w^2-1} \Big|_{w=\frac{\alpha-u}{\beta}+1} \frac{du}{\beta} \frac{1}{\exp(u)+1} \\ & + \int_0^{\infty} w\sqrt{w^2-1} \Big|_{w=\frac{v+\alpha}{\beta}+1} \frac{dv}{\beta} \frac{1}{\exp(v)+1}. \end{aligned} \quad (3.89)$$

The first integral of equation (3.89) gives a contribution of the order  $(\frac{\alpha}{\beta})^3$ :

$$\int_1^{w_0} w\sqrt{w^2-1} dw = \frac{1}{3}(w_0^2-1)^{3/2} = \frac{1}{3} \left( \frac{\alpha^2}{\beta^2} - 2\frac{\alpha}{\beta} \right)^{3/2}. \quad (3.90)$$

The contribution of the other two integrals is significantly smaller.

For the first part of the integrand in the last integral in (3.89) we use the expansion

$$w\sqrt{w^2-1} \Big|_{w=\frac{v+\alpha}{\beta}+1} = \frac{\alpha^2}{\beta^2} + \frac{2(v+\beta)}{\beta} \frac{\alpha}{\beta} + \left( \frac{1}{2} + \frac{v^2}{\beta^2} + \frac{2v}{\beta} \right) - \frac{1}{8} \frac{\beta^2}{\alpha^2} + \mathcal{O}\left(\frac{\beta^3}{\alpha^3}\right). \quad (3.91)$$

In the calculation we neglect the higher order terms since even  $-\frac{1}{8} \frac{\beta^2}{\alpha^2}$  has only a marginal contribution at the assumed large values for  $\alpha$ . In addition we have to consider the second part of the integrand. We use the correlation

$$\int_0^{\infty} dv \frac{v^n}{1+\exp(v)} = (1-2^{-n})\Gamma(1+n)\zeta(1+n), \quad (3.92)$$



with

$$\int_0^\infty \frac{dv}{1+\exp(v)} = \log(2), \quad \int_0^\infty \frac{v dv}{1+\exp(v)} = \frac{\pi^2}{12}, \quad \int_0^\infty \frac{v^2 dv}{1+\exp(v)} = \frac{3\zeta(3)}{2}, \quad (3.93)$$

where  $\zeta$  is the Riemann zeta function and  $\zeta(3) \approx 1.20206\dots$ . The combination of both parts, the first and the second, leads to the expansion of the respective integral,

$$\begin{aligned} \int_0^\infty w \sqrt{w^2 - 1} \Big|_{w=\frac{v+\alpha}{\beta}+1} \frac{dv}{\beta} \frac{1}{\exp(v)+1} \\ \approx \frac{\alpha^2}{\beta^2} \frac{\log(2)}{\beta} + \left( \frac{\pi^2}{6\beta^2} + \frac{2\log(2)}{\beta} \right) \frac{\alpha}{\beta} + \left( \frac{\log(2)}{2\beta} + \frac{3\zeta(3)}{2\beta^3} + \frac{\pi^2}{6\beta^2} \right). \end{aligned} \quad (3.94)$$

This leaves the second integral of (3.89) to be inspected. Again the first part of the integrand is expanded:

$$w \sqrt{w^2 - 1} \Big|_{w=\frac{\alpha-u}{\beta}+1} = \frac{\alpha^2}{\beta^2} + \frac{2(\beta-u)}{\beta} \frac{\alpha}{\beta} + \left( \frac{1}{2} + \frac{u^2}{\beta^2} + \frac{2u}{\beta} \right) - \frac{1}{8} \frac{\beta^2}{\alpha^2} + \mathcal{O}\left(\frac{\beta^3}{\alpha^3}\right). \quad (3.95)$$

If for the second part we set the upper boundary of the integral to infinity due to the assumed large  $\alpha$ , in combination with the above expansion we obtain an expression similar to the last integral of (3.89):

$$\begin{aligned} - \int_0^\alpha w \sqrt{w^2 - 1} \Big|_{w=\frac{\alpha-u}{\beta}+1} \frac{du}{\beta} \frac{1}{\exp(u)+1} \approx - \int_0^\infty w \sqrt{w^2 - 1} \Big|_{w=\frac{\alpha-u}{\beta}+1} \frac{du}{\beta} \frac{1}{\exp(u)+1} \\ \approx - \frac{\alpha^2}{\beta^2} \frac{\log(2)}{\beta} - \left( \frac{2\log(2)}{\beta} - \frac{\pi^2}{6\beta^2} \right) \frac{\alpha}{\beta} - \left( \frac{\log(2)}{2\beta} + \frac{3\zeta(3)}{2\beta^3} - \frac{\pi^2}{6\beta^2} \right). \end{aligned} \quad (3.96)$$

To show that the approximation error from the used expansion is negligible, we use the connection [OLBC10]

$$\Gamma(s, z) = \int_z^\infty t^{s-1} e^{-t} dt \approx z^{s-1} e^{-z}, \quad (3.97)$$

which is valid for large  $z$ . We apply this to the neglected integral over  $u$  within the boundaries  $\alpha$  and  $\infty$  of the Fermi distribution times  $u$  to the power of  $n$ ,  $n$  being 0, 1 and 2. With  $u = \alpha - \beta(w-1) \gg 0$  our result reads

$$\frac{1}{\beta} \int_\alpha^\infty \frac{u^n du}{\exp(u)+1} \leq \frac{1}{\beta} \int_\alpha^\infty u^n \exp(-u) = \frac{1}{\beta} \Gamma(n+1, \alpha) \approx \frac{1}{\beta} \alpha^n e^{-\alpha}, \quad (3.98)$$

which is exponentially small for every occurring  $n$  ( $n = 1, 2, 3$ ) and justifies our approximation.

The derived expressions for the three integrals of (3.89) combine to

$$F_r(\alpha) = \int_1^\infty \frac{w \sqrt{w^2 - 1}}{\exp(\beta(w-1) - \alpha) + 1} dw \approx \frac{1}{3} \left[ \left( \frac{\alpha}{\beta} + 1 \right)^2 - 1 \right]^{3/2} + \frac{\pi^2}{3\beta^2} \frac{\alpha}{\beta} + \frac{\pi^2}{3\beta^2}. \quad (3.99)$$

We use this expression for  $F_r(\alpha)$  in the region where it works most accurately: close to the nucleus where  $y$  (correspondingly, the nuclear potential  $\Phi_r$  derived from relativistic considerations) is large (e.g.  $y \geq 35$  in the considered plasma environment). The function  $Y_r(x)$  is derived in this case via (3.81).

### 3.3.2.3 Expansion Far From the Nucleus

For the opposite direction—far from the nucleus—where  $y$  is small, the expansion goes analog to the non-relativistic treatment:

$$\begin{aligned}
 F_r(\eta + y) &\approx \int_1^\infty \frac{w\sqrt{w^2 - 1}dw}{\exp(\beta(w - 1) - (\eta + y)) + 1} \\
 &\approx F_r(\eta) + \left. \frac{dF_r(\eta + y)}{dy} \right|_{y=0} \cdot y \\
 &= F_r(\eta) + \int_1^\infty w\sqrt{w^2 - 1}dw \left. \frac{d}{dy} \frac{1}{\exp(\beta(w - 1) - (\eta + y)) + 1} \right|_{y=0} \cdot y \\
 &= F_r(\eta) + \int_1^\infty \frac{\exp(\beta(w - 1) - (\eta + y))w\sqrt{w^2 - 1}dw}{(\exp(\beta(w - 1) - (\eta + y)) + 1)^2} \Big|_{y=0} \cdot y \\
 &= F_r(\eta) + \left( \int_1^\infty \frac{(\exp(\beta(w - 1) - \eta) + 1)w\sqrt{w^2 - 1}dw}{(\exp(\beta(w - 1) - \eta) + 1)^2} \right. \\
 &\quad \left. - \int_1^\infty \frac{w\sqrt{w^2 - 1}dw}{(\exp(\beta(w - 1) - \eta) + 1)^2} \right) \cdot y \\
 &= F_r(\eta) + yF_r(\eta) - y \int_1^\infty \frac{w\sqrt{w^2 - 1}dw}{(\exp(\beta(w - 1) - \eta) + 1)^2}. \tag{3.100}
 \end{aligned}$$

The last integral in the expression above is less than 0.0001 for all  $\eta \leq -2$  and vanishes very fast for even smaller  $\eta$ . Thus, similar to the non-relativistic Poisson equation we obtain

$$\frac{d^2}{dx^2} Y_r(x) \approx \frac{x}{1 + j^*} \left[ \frac{F_r(\eta) + Y_r(x)/xF_r(\eta)}{F_r(\eta)} - 1 \right] = \frac{x}{1 + j^*} Y_r(x)/x \approx Y_r, \tag{3.101}$$

and

$$Y_r(x) = Ce^{-x}, \tag{3.102}$$

$$y_r(x) = \frac{C}{x} e^{-x}, \tag{3.103}$$

with  $C = Y_r(x_{r,\text{fix}})/e^{-x_{r,\text{fix}}}$  for a fixed value  $x_{r,\text{fix}}$ . Again we calculate  $Y_r(x_{r,\text{fix}})$  from the numerical solution of the Poisson equation (including here the approximation in the nucleus region, too) after choosing the merging point  $x_{r,\text{fix}}$ .

### 3.3.2.4 Quantum Mechanical Corrections

Within the relativistic treatment a correction to the Fermi model is indispensable. While the non-relativistic Poisson equation was solvable even without the quantum mechanical corrections,

here this is no longer possible. The local electron density becomes singular to the extent that it cannot be integrated [AH70]. In order to circumvent this problem, we include the quantum mechanical considerations that correct the behavior of the electron density at the origin as done before in section 3.3.1.4. We will restrict ourselves to the non-relativistic correction in the following. The relativistic treatment of the quantum mechanical correction is expected to have a small effect on the ionization states of osmium and is numerically cumbersome. A full approach can be found in [AH70].

The construction of the applied quantum mechanical correction is absolutely parallel to the one depicted in section 3.3.1.4 leading to  $Y_{r,\text{qm}}$ . It altogether results in

$$y_r(x) = \begin{cases} Y_{r,\text{qm}}(x)/x & \text{for } x \leq x_{r,0}, \\ Y_{r,\text{num}}(x)/x & \text{for } x_{r,0} \leq x \leq x_{r,\text{fix}}, \\ Y_{r,\text{approx}}(x)/x & \text{for } x_{r,\text{fix}} \leq x, \end{cases} \quad (3.104)$$

where  $Y_{r,\text{approx}}$  denotes the solution of (3.102) and  $Y_{r,\text{approx}}$  is given by (3.81) with the Fermi integral expression (3.99) for high  $y$ .

### 3.3.2.5 Perturbing Potential

To get the perturbing potential  $v_r$  of the free plasma electrons, we once again have to constrain the local electron number density to electrons whose kinetic energies exceed the energy needed to overcome the nuclear potential. The lower boundary of the integral therefore needs to be in accordance with the condition  $\beta(w-1) = y \Rightarrow w = \frac{y}{\beta} + 1$  (kinetic energy equals the potential energy of the nucleus) [TY83]:

$$\begin{aligned} n_{e,r,\text{pert}}(r) &= \frac{8\pi m_e^3 c^3}{h^3} \int_{1+\frac{y}{\beta}}^{\infty} \frac{w\sqrt{w^2-1}}{\exp(\beta(w-1) - (\eta+y)) + 1} dw = \frac{8\pi m_e^3 c^3}{h^3} G_r(\eta+y, y) \\ &= n_{e,r}(\infty) \frac{G_r(\eta+y, y)}{F_r(\eta)}. \end{aligned} \quad (3.105)$$

Now the Poisson equation for the perturbing potential can be formulated as

$$\frac{1}{x} \frac{\partial^2}{\partial x^2} (x v_r) = \frac{1}{j^* + 1} \left[ \frac{G_r(\eta+y, y)}{F_r(\eta)} - \langle e^{-jy} \rangle \right] =: S_r(x), \quad (3.106)$$

with the initial conditions that  $v_r$  should be finite and its derivative constant at the origin. At infinite distance from the nucleus,  $v_r$  should again become zero, leading all its other values to be negative. Since  $S_r(x)$  is dependent on  $y_r(x)$ , we compute  $S_r(x)$  with the help of equation (3.104).

Also in this case an approximation of  $G_r(\eta+y, y)$  is desirable. Furthermore, it would be advantageous if we could follow the procedure we applied to the last integral in (3.89). To this end we make the substitution

$$u := w - 1 - \frac{y}{\beta} \Rightarrow w = 1 + u + \frac{y}{\beta}, \quad \frac{du}{dw} = 1 - \frac{y}{\beta}, \quad (3.107)$$

that gives a lower boundary of zero for the integral:

$$G_r(\eta+y, y) = \int_0^{\infty} w \sqrt{w^2-1} \Big|_{w=1+u+\frac{y}{\beta}} \frac{du}{\exp(\beta u - \eta) + 1}. \quad (3.108)$$

The similarity between the right hand side of this equation and the already expanded integral in (3.89) is now obvious. Thus we follow the procedure in section 3.3.2.2, that begins with equation (3.91). First we expand the first part of the integrand:

$$w\sqrt{w^2-1}\Big|_{w=1+u+\frac{y}{\beta}} = \frac{y^2}{\beta^2} + \frac{2(1+u)y}{\beta} + \left(\frac{1}{2} + 2u + u^2\right) - \frac{\beta^2}{8y^2} + \mathcal{O}\left(\frac{1}{y^3}\right). \quad (3.109)$$

We neglect terms of the order of  $\frac{1}{y^3}$ , for we consider  $G_r(\eta + y, y)$  in a region close to the nucleus, where its potential energy  $y$  (in terms of  $\kappa T$ ) is high. Including the second part of the integrand we obtain integrals of the form

$$U_n := \int_0^\infty \frac{u^n}{\exp(\beta u - \eta) + 1} du, \quad n = 0, 1, 2, \quad (3.110)$$

which have definite values. In combination with the above expansion, we obtain

$$G_r(\eta + y, y) \approx \frac{y^2}{\beta^2} U - 0 + 2\frac{y}{\beta}(U_0 + U_1) + (U_2 + 2U_1 + \frac{1}{2}U_0) - \frac{\beta^2}{8y}U_0, \quad (3.111)$$

which we apply within  $S_r(x)$  for large values of  $y$  (e.g.  $y \geq 100$ ) to save computational time.

After performing the relativistic calculation of the nuclear potential and considering the expansion used in the derivation of the perturbing potential as a function of the nuclear potential, finally, the continuum depression for the relativistic treatment (see [TY83]) reads

$$\Delta_{r,j} = \kappa T v_r(0) = -\kappa T \int_0^\infty t S_r(t) dt. \quad (3.112)$$

Our corrected ionization potential needed as input for the Saha equation then is given by

$$\chi_{i,j} = I_{i,j} - \Delta_{r,j}. \quad (3.113)$$

With this, we have now everything we need to calculate the partition functions and we can proceed to solve the Saha equation. Our numerical results for osmium in different plasma environments are described in the next chapter.

## 4 Numerical Results for Os

The aim of our calculations is to check the validity of the assumption in [Hel11] that the K-shell or the L-shell of the osmium isotope in the plasma are free. This would be the case if the osmium isotope is highly enough ionized for those shells to be unoccupied by bound electrons. In this chapter we proceed to calculate the degree of ionization for osmium in the characteristic plasma environments described in section 2.4 and present our numerical results.

### 4.1 Self-Consistent Method

We have chosen our test case as the plasma composition a) of section 2.4 with mass fractions  $x_{\text{He}} = 0.78$  (78% He),  $x_{\text{C}} = 0.20$  (20% C), and  $x_{\text{O}} = 0.02$  (2%O), together with a temperature of  $T = 3 \cdot 10^8$  K, which is comparatively high for the s-process. By means of this example we detail step by step our calculations. However, before that, we explain the additional approximations that will be used.

#### 4.1.1 Approximations Within the Saha Equation

Due to the high mass of the nucleons compared to those of the electrons, we can use the atom masses instead of the ion masses, as we already pointed out at the end of section 3.2. Thus, the quotient  $\left(\frac{m_{i,j+1}}{m_{i,j}}\right)^{\frac{3}{2}}$  in the Saha equation (3.1) becomes equal to one. Also the ion number densities of equation (3.29) in section 3.2 can now be calculated easier via

$$\sum_j n_{i,j} = \frac{\rho x_i}{m_i}. \quad (4.1)$$

Still, the ionization distribution needed for the sum in this equation calls for a self-consistent method. A good approximation is to act on the assumption that the plasma ions (H-, He, C-, O-ions) are fully ionized. For the assumed temperatures the available energy ( $\kappa T$ ) ranges between 7.756 keV and 30 keV. The uncorrected ionization potentials of the considered four plasma ion species  $i$  are of the order of maximally 1 keV. Corrections due to the continuum lowering even enhance the ionization. Thus, we can safely assume a full ionization of H, He, C and O. The ion number densities  $n_{i,j}$  then simply derive from

$$n_{i,j} = n_i = \frac{\rho x_i}{m_i}. \quad (4.2)$$

Additionally, we can specify the average ionization of the plasma as defined by equation (3.42)

$$j^* = \frac{\sum_i Z_i^2 n_i}{\sum_i Z_i n_i}. \quad (4.3)$$

We now consider the partition function  $b_{i,j}$ , more precisely its components (see equation (3.20)): the statistical weight  $b_{i,j,k}$  and the excitation energies  $\epsilon_{i,j,k}$ . For both parameters we

follow the schematic model constructed by Takahashi and Yokoi in Appendix B of Ref. [TY83]. They make the simplification to assume single-particle electrons filling up the orbits of the respective ion according to the serial order of the principal quantum number and of the orbital quantum number. We now denote the ground state outer principal quantum numbers with  $n$  (not to be mistaken for the number density) and the outer orbital quantum number with  $l$ . The number of electrons in  $l$  we call  $N$ . According to [TY83] the statistical weight is then calculated via

$$b_{i,j,k} = \begin{cases} B_0(l, N) & \text{for } k = 0, \\ B_1(n, l, N) & \text{for } k = 1, \\ B_2(n, l, N, k) & \text{for } k > 0, \end{cases} \quad (4.4)$$

with

$$B_0(l, N) = \frac{(2(2l+1))!}{N!(2(2l+1)-N)!}, \quad (4.5)$$

$$B_1(n, l, N) = \frac{(2n^2)!}{(2l^2+N)!(2n^2-2l^2-N)!} - B_0(l, N), \quad (4.6)$$

$$B_2(n, l, N, k) = \frac{2(n+k-1)^2(2n^2)!}{(2l^2+N-1)!(2n^2-2l^2-N+1)!}. \quad (4.7)$$

By applying the hydrogen-like model formula to the outer bound excited electron, we obtain for the excitation energies

$$\epsilon_{i,j,k} = \begin{cases} 0 & \text{for } k = 0 \text{ or } j = Z_i, \\ I_{i,j} - \frac{Ry(j+1)^2}{(n+k-1)^2} & \text{for } k \neq 0, j \neq Z_i. \end{cases} \quad (4.8)$$

Here,  $I_{i,j}$  is the uncorrected ionization potential; as in section 3.1, equations (3.18), (3.22), (3.24) and (3.25),  $Z_i$  denotes the proton number of the atom  $i$  and  $Ry$  denotes the Rydberg unit of energy,  $Ry = 13.60569253$  eV [MTN08]. The cut-off integer for the summation within the partition function is calculated as the highest value for  $k$  for which  $\epsilon_{i,j,k}$  is still smaller than the respective value  $\chi_{i,j} = I_{i,j} - \Delta_j$ .

### 4.1.2 Detailed Calculation For One Configuration

Let our plasma now consist of 78% helium, 20% carbon and 2% oxygen, corresponding to the mass fractions  $x_{He} = 0.78$ ,  $x_C = 0.20$ , and  $x_O = 0.02$ . This correlates to the composition of the carbon pocket in the intershell of a TP-AGB star, where the s-process of heavy elements like osmium take place, see section 2.4. As mass density we consider  $\rho = 10^3 \text{ g/cm}^3$ , and as temperature we assume  $T = 3 \cdot 10^8$  K. In the temperature range of the s-process between  $0.9 \cdot 10^8$  K and  $3 \cdot 10^8$  K, this corresponds to the upper limit but follows former assumptions in the literature for the classical s-process model.

Before we can solve the Saha equation we first need to calculate the degeneracy parameter  $\eta$ , respectively  $a$ , i.e., the chemical potential, and the continuum depression, by following the steps outlined in section 3.3.

#### 4.1.2.1 Chemical Potential

To get the chemical potential and thus the degeneracy parameter as derived in section 3.2, we calculate the electron density of the plasma (3.30) with the help of (4.2):

$$n_e = \rho \sum_{i,j} j n_i = \rho \sum_i Z_i \frac{x_i}{m_i} = \rho \left( 2 \frac{x_{He}}{m_{He}} + 6 \frac{x_C}{m_C} + 8 \frac{x_O}{m_O} \right) = 3.00964 \cdot 10^{32} \text{ cm}^{-3}. \quad (4.9)$$

As a next step we find the value  $\eta$  by equalizing  $n_e$  from above with  $n_e(\eta)$  from equation (3.28). We obtain

$$\eta = -4.51221. \quad (4.10)$$

For the non-relativistic case we need  $a$  ( $= \frac{\mu_e}{\kappa T}$ ) instead of  $\eta$ . Therefore, we equalize  $n_e = 3.00964 \cdot 10^{32} \text{cm}^{-3}$  and  $n_e(\infty, a)$  from equation (3.33) with the result

$$a = 4.41916. \quad (4.11)$$

With  $\eta$  and  $a$  we are now able to address the continuum depression.

#### 4.1.2.2 Continuum Depression

We calculate the continuum depression for our model configuration for both relativistic and non-relativistic cases. A comparison shows a noticeable energy difference. For the other considered plasma configurations we will restrict ourselves to the generally valid relativistic treatment and present only the final results.

#### Non-Relativistic Case

To begin with, we calculate the parameters that characterize our plasma. The average ionization of the plasma is

$$j^* = 2.91971, \quad (4.12)$$

and its Debye-length amounts to round 66% of the Bohr radius

$$D = 3.48002 \cdot 10^{-11} \text{m}. \quad (4.13)$$

Our next aim is to derive the nuclear potential  $\Phi$ , or rather  $y = \frac{e\Phi}{\kappa T}$ , for the osmium ion in the plasma. The boundary condition of the Poisson equation (3.44) for  $x \rightarrow 0$  reads

$$Y_0 = xy(x)|_{x=0} = \frac{Ze^2}{\kappa T} = 0.121644. \quad (4.14)$$

To solve the Poisson equation we split the expression of the fraction  $\frac{F_{nr}(y+a)}{F_{nr}(a)}$  in three intervals. For  $y < 35$  we consider the exact ratio, while for other  $y$  we use the approximation in (3.45) to save computational time. The discrepancy amounts to less than 5% at  $y = 35$ , which is good enough for our purpose—considering that even for higher values of  $y$  we do not obtain a better agreement between the approximation and the exact ratio. With this expression we solve the Poisson equation in a self-consistent way to get  $Y(x)$ , i.e., we use a loop to calculate the interdependent parameters: the slope  $C$  of  $Y(x)$  in the point  $x_{\text{fix}}$ , where instead of the numerical solution we start to apply  $Y_{\text{approx}}(x) = Ce^{-x}$  for higher  $y$ , and the value of the boundary condition of the differential equation that  $Y_{\text{num}}(x_{\text{fix}}) = -Y_{\text{num}}'(x_{\text{fix}})$  due to the validity of this condition for  $Y_{\text{approx}}(x_{\text{fix}})$ . We choose  $x_{\text{fix}} = 8$ , where the approximation (3.51) holds with only  $3.77 \cdot 10^{-5}$  discrepancy. The slope there is  $C = 0.128537$  and the value of the boundary condition  $Y_{\text{num}}(x_{\text{fix}}) = 4.312 \cdot 10^{-5}$ . Additionally, we merge the asymptotic expression (3.47) at  $x = 0.0001$ , whose slope  $s$  is thus determined to be  $s = -0.183388$ .

In the following, we denote the resulting solution  $Y(x)$  with  $\tilde{Y}_{nr}$ , where  $nr$  specifies the non-relativistic case and the  $\sim$  stands for the treatment without quantum mechanical corrections.

The quantum mechanical corrected solution is derived in a similar way, with two differences. On the one hand, for small  $y$  we apply the quantum mechanical asymptotic expression (3.55)

instead of the linear approximation in (3.47). On the other hand, we must also find the corresponding merging point  $x_0$  as described in section 3.3.1.4. The three interdependent parameters have to be aligned. Again a computational loop solves this problem self-consistently. Correspondingly, we denote the solution of the Poisson equation (equation (3.63) multiplied by  $x$ ) with  $Y_{\text{nr}}$  and show its behavior as a function of  $x$  (the radius in units of the Debye-length) in Figure 4.1. The difference compared to the uncorrected version  $\tilde{Y}_{\text{nr}}$  is only visible for an ex-

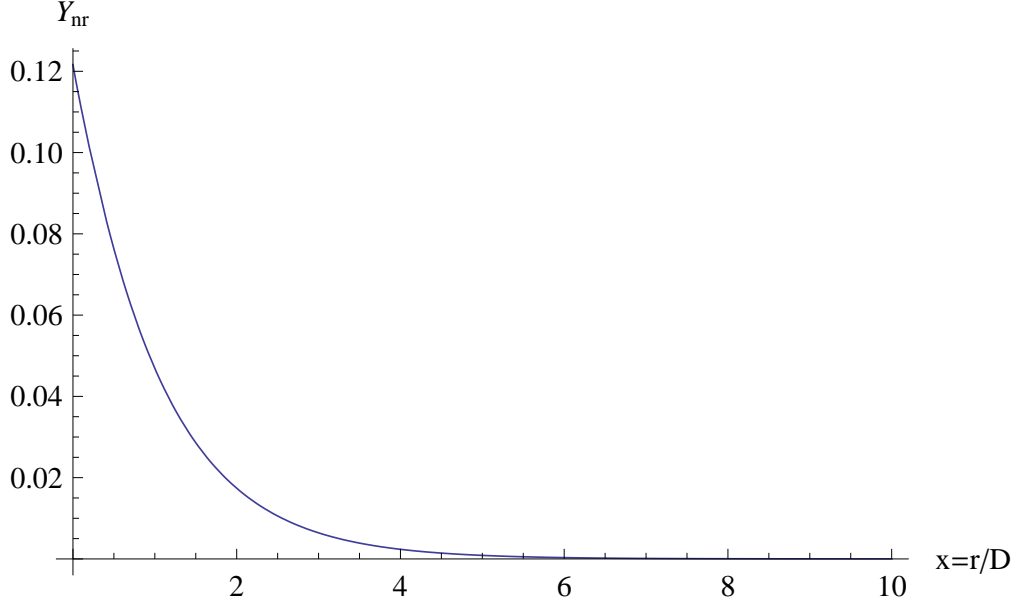


**Figure 4.1:** Non-relativistic solution  $Y_{\text{nr}}$  of the Poisson equation (3.44) calculated using plasma mass fractions  $x_{He} = 0.78$ ,  $x_C = 0.20$ ,  $x_O = 0.02$  for an osmium ion in a stellar plasma at  $T = 3 \cdot 10^8$  K.

cerpt close to the origin, as shown in Figure 4.2, for the radius in units of the Debye-length  $x \in [0, 0.05]$ .

The results  $\tilde{Y}_{\text{nr}}$  and  $Y_{\text{nr}}$  divided by  $x$  (to get  $y$ ) can then be plugged into the expression of  $S(x)$  in equation (3.65). With the help of equation (3.76) the net ionic charge of osmium in the considered plasma calculated via the Fermi model can be obtained,

$$\tilde{Z}^* = \frac{D\kappa T}{e^2} \int_0^\infty t^2 \tilde{S}(t) dt = 72.6354, \quad (4.15)$$

$$Z^* = \frac{D\kappa T}{e^2} \int_0^\infty t^2 S(t) dt = 72.968. \quad (4.16)$$

The uncorrected and corrected version show a difference of  $\frac{1}{3}$  bound electrons. Both models agree that less than four bound electrons are left in the osmium atomic shells. This result will be compared with the result from the Saha equation.

As a further interesting result, we can “count” the innermost electrons, i.e., the electrons, who fill the ion’s orbits between the assumed point-like nucleus at  $x = 0$  and the derived value  $x_0 = 0.0358098$ . In this region the quantum mechanical solution of the Poisson equation is effective. We denote this number with  $N_{e,\text{nr}}$  and calculate it by multiplying the corresponding volume with the electron number density, which in the quantum mechanical case is given by



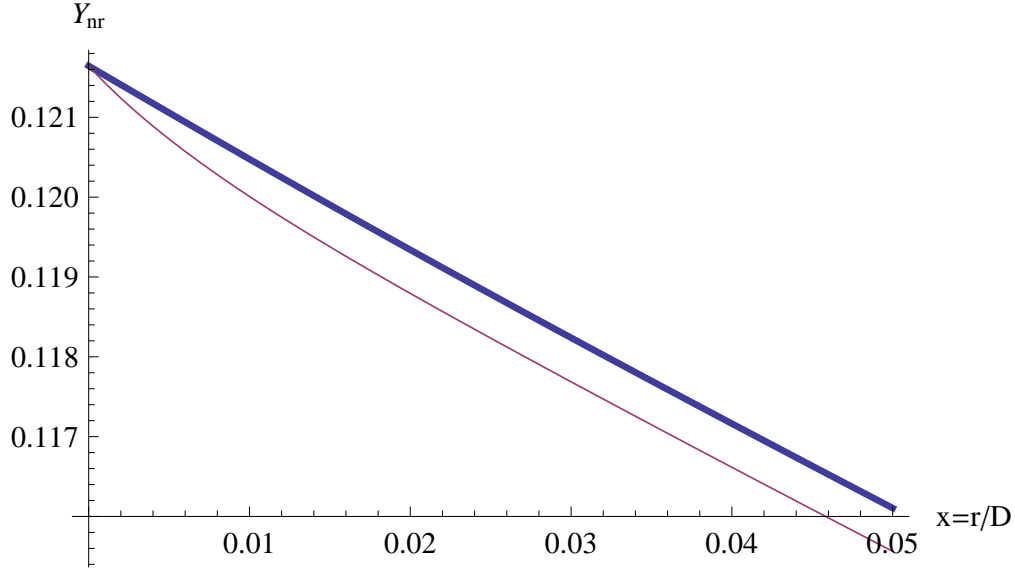


**Figure 4.2:** Comparison between the non-relativistic solution of the Poisson equation with ( $Y_{\text{nr}}$ , thick blue line) and without ( $\tilde{Y}_{\text{nr}}$ , thin violet line) including the quantum mechanical correction.

$Ae^{-By}$ . Without the quantum mechanical correction the local electron density of the bound state electrons is derived essentially in the same way as the perturbing density  $G_{\text{nr}}$  (see section 3.3.1.5). However, instead of accounting for electrons whose kinetic energy exceeds the nuclear potential energy, we now only include those with kinetic energy less than the nuclear potential energy ( $z < y$ ). The Fermi integral for this case is then  $H_{\text{nr}}(y+a, y) = F_{\text{nr}}(y+a) - G_{\text{nr}}(y+a, y)$ . The results, for which we convert  $r$  to  $x$  ( $r = Dx$ ,  $dr = Ddx$ ), show the difference between the uncorrected and the corrected treatment:

$$\tilde{N}_{\text{e,nr}} = V\tilde{n}_{\text{nr}}(r) = 4\pi D^3 \int_0^{x_0} n_{\text{e}}(\infty) \frac{H_{\text{nr}}(\tilde{Y}_{\text{nr}}(x)/x + a, \tilde{Y}_{\text{nr}}(x)/x)}{F_{\text{nr}}(a)} x^2 dx = 0.459432, \quad (4.17)$$

$$N_{\text{e,nr}} = Vn_{\text{nr}}(r) = 4\pi D^3 \int_0^{x_0} n_{\text{e}}(\infty) Ae^{-BY_{\text{nr}}(x)/x} x^2 dx = 0. \quad (4.18)$$

Effectively, the uncorrected version shows about half an electron in the innermost region of the osmium ion's orbits, where the corrected version sees none. Such discrepancies are bound to occur since the Fermi model is not appropriate for describing bound state electrons. The difference between quantities calculated with and without the quantum mechanical correction is even bigger here than the one for the effective charge of the ion (4.15)-(4.16), implying that the error gets slightly corrected with growing distance to the nucleus.

Finally, with equation (3.77) we compute the continuum depression for our osmium ion in the considered plasma environment once uncorrected, once with the quantum mechanical correction,

which accounts for an additional lowering of about 10 eV:

$$\tilde{\Delta}_j = \kappa T \int_0^\infty t \tilde{S}(t) dt = 2441.22 \text{ eV}, \quad (4.19)$$

$$\Delta_j = \kappa T \int_0^\infty t S(t) dt = 2451.26 \text{ eV}. \quad (4.20)$$

Since the uncorrected ionization potentials of osmium range from 8.73 eV to 83.78 keV [Spe12], already the pressure ionization would account for an ionization of  $j = 46$ . Together with the energy  $\kappa T = 28.293$  keV, an ionization in the region of  $j = 74$  should occur. The more accurate average ionization degree of osmium will be obtained by solving the Saha equation, but before that we derive the relativistic result for the continuum depression.

### Relativistic Case

With the same parameter  $j^*$ ,  $D$ , and  $Y_0$  and the method described in section 3.3.2 and above for the non-relativistic, quantum mechanical corrected case, we derive the solution  $Y_r(x)$  of the Poisson equation (3.81). Again we choose  $x_{\text{fix}} = 8$  as the point where we merge the exponential form of  $Y_r(x)$  due to the expansion far from the nucleus (see section 3.3.2.3) to the numerical results for the central region. The self-consistent calculation gives  $x_0 = 0.0359729$  as transit point for the quantum mechanical solution (3.55). If we divide our solution by  $x$  we get the  $y_r$  as in equation (3.104), i.e., the nuclear potential energy in units of  $\kappa T$ .

We plug  $y_r$  in the expression of  $G_r$  (the approximation (3.111) we use for  $y_r \geq 5\beta \approx 100$ ) to receive  $S_r(x)$  as in (3.106). Again we are able to determine the effective ionic charge of the osmium ion as calculated from the Fermi model according to (3.76):

$$Z_r^* = \frac{D\kappa T}{e^2} \int_0^\infty t^2 S_r(t) dt = 73.2026. \quad (4.21)$$

This corresponds to 2.7974 bound electrons. In the region  $x \leq x_0$  we find 0 bound electrons, which we computed as in (4.18), only with  $Y_r(x)$  instead of  $Y_{\text{nr}}(x)$ .

From our relativistic calculation a continuum depression of

$$\Delta_j = \kappa T \int_0^\infty t S_r(t) dt = 2478.71 \text{ eV} \quad (4.22)$$

arises. This again accounts for 46 electrons already ionized due to pressure ionization.

### Comparison Between the Non-Relativistic and Relativistic Case

In our comparison, we only use the quantum mechanical corrected version for the non-relativistic case. The differences between the corrected and the uncorrected treatment were shown already in section 4.1.2.2.

The solutions we receive from the relativistic and corrected non-relativistic Poisson equation,  $Y_r(x)$  and  $Y_{nr}(x)$ , are so similar that the plots of both functions appear to be identical. We refer to Figure 4.1. The following table summarizes the results that characterize the non-relativistic and the relativistic calculation concerning the continuum depression.

Calculation Mode	$\Delta_j$ [eV]	$Z^*$	$N_e$	$x_0$
<b>nr</b>	2451.26	72.968	$9.18 \cdot 10^{-97}$	0.0358098
<b>r</b>	2478.71	73.2026	$21.85 \cdot 10^{-97}$	0.0359729

**Table 4.1:** Comparison between the non-relativistic (nr) and the relativistic (r) calculation concerning the continuum depression  $\Delta_j$ , the effective charge of the ion  $Z^*$ , the number of the bound electrons between the nucleus and  $x_0$  and the merging point  $x_0$ , where the quantum mechanical modification meets the purely numerical form of  $Y(x)$ ,  $Y_r(x)$  respectively.

The merging points  $x_0$  are close together. In both cases there are effectively zero bound electrons between the nucleus and  $x_0$ , which was expected, since we have used the same quantum mechanical correction, i.e., have fitted the same form of function to the purely numerical central part of  $Y$ . The values  $x_0$  of the non-relativistic (nr) and the relativistic (r) case correspond to the radii  $r_{nr,0} = 1.24619 \cdot 10^{-12}$  m and  $r_{r,0} = 1.25186 \cdot 10^{-12}$  m, respectively. Using the simple Bohr atomic model and the Bohr radius  $a_0$ , the radius ascribed to the K-shell of the hydrogen-like osmium ion is

$$r_K = \frac{a_0}{Z} = 6.96286 \cdot 10^{-13}, \quad (4.23)$$

which is smaller than both radii  $r_{nr,0}$  and  $r_{r,0}$ . We can therefore safely assume that the K-shells of the osmium ions are unoccupied. Furthermore, even the L-shells will only be partly occupied. The effective ion charges  $Z^*$  show a discrepancy of less than  $\frac{1}{4}$  bound electrons, that are absent in the relativistic case. The biggest difference appears in the continuum depression with a difference of 27.45 eV, showing that the plasma electrons call for a relativistic treatment even though the thermal energy  $\kappa T = 25.852$  keV is 20 times less than the rest energy of the electron.

#### 4.1.2.3 Ionization State

With the ionization potentials from [Spe12], the schematic shell configurations as described in 4.1.1, the degeneracy parameter and the calculated continuum depression, we have every ingredient to solve the Saha equation (3.1). In a recurrence loop we do so for every ionization state  $j$  from 1 to  $Z = Z_{Os}$  and set the value for the number density of the neutral atom  $n_{Os,0}$  to one. The results are collected and summed over, and out of these values the ionization number fractions, i.e. the individual results for a certain  $j$  divided by their sum, are calculated. We list our results in Table 4.2 and illustrate them in Figure 4.3.

Ionization State $j$	$\leq 70$	71	72	73	74	75	76
nr: $n_{Os}$ [%]	$\sim 0$	0.038	0.477	2.676	22.183	50.286	24.338
r: $n_{Os}$ [%]	$\sim 0$	0.026	0.360	2.221	20.226	50.377	26.788

**Table 4.2:** Distribution of the relative osmium ion number densities (in %) as function of the ionization degree  $j$  for the non-relativistic and relativistic calculation. The used plasma configuration is the same as in Figures 4.1 and 4.2.

For both calculation modes—non-relativistic and relativistic—we have about 25% bare osmium nuclei. Over half have only one bound electron left, about one fifth still have two bound electrons. The rest accounts for around 3%. Corresponding to the higher continuum depression,

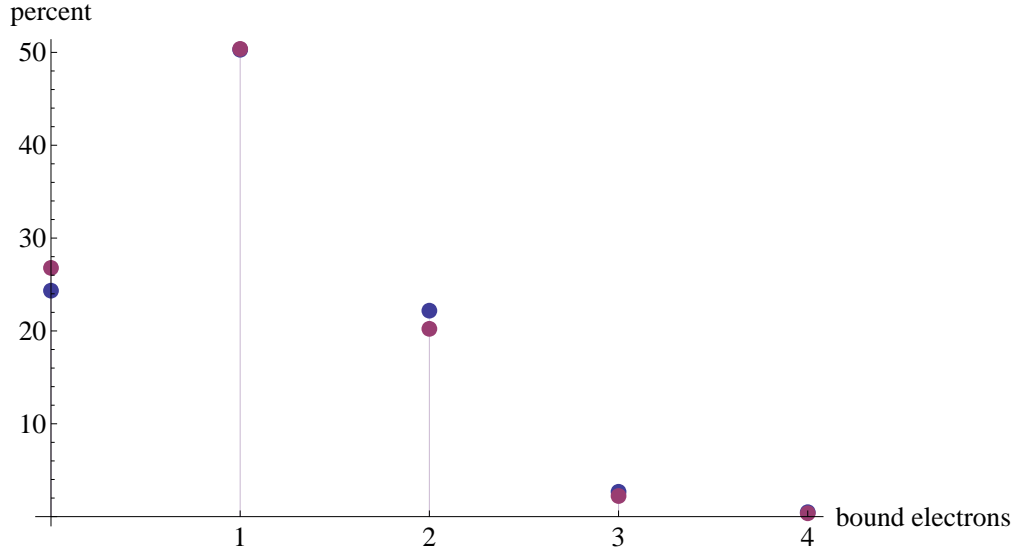


**Figure 4.3:** Ionization states of osmium in percent as resulting from the Saha equation for the model plasma configuration a) from 2.4 at  $T = 3 \cdot 10^8$  K. Red dots stand for the relativistic, blue dots for the non-relativistic calculation. The abscissa shows the number of bound electrons, where 0 refers to a fully ionized osmium ion.

in the relativistic computation method the ionization degree is higher than the one derived from the non-relativistic method ( $\bar{j}_r > \bar{j}_{nr}$ ).

The averaged ionization degrees are

$$\bar{j}_{nr} = 74.9521, \quad (4.24)$$

$$\bar{j}_r = 75.0093. \quad (4.25)$$

Compared to those derived from the Fermi model (see (4.16) and (4.21)), the values calculated here via the Saha equation are about two ionization degrees higher. This discrepancy can be explained by the fact that the Fermi model cannot properly describe bound states. The results delivered by the Saha equation, on the other hand, treat the ionization process in the plasma accurately and provide the correct results.

For the other plasma and temperature configurations we restrict ourselves to the relativistic computation method since it is of more general validity.

#### 4.1.3 Results For All Configurations

We have performed the calculation for all specified plasma configurations, each case for the extremal temperatures,  $T = 0.9 \cdot 10^8$  K and  $T = 3.48 \cdot 10^8$  K. The resulting relative osmium ion number densities for  $T = 0.9 \cdot 10^8$  K are distributed between  $j = 66$  and  $j = 74$ , whereas for  $T = 3.48 \cdot 10^8$  K they range from  $j = 71$  to  $j = 76$ . The values in percent are listed in Tables 4.3 and 4.4.

We note that plasma composition b) (73% He, 25% C, 2%O) gives the highest ionization degrees, whereas an osmium ion in composition d) would be significantly less ionized. This is illustrated by the averaged ionization states shown in Table 4.5.

Ionization State $j$	66	67	68	69	70	71	72	73	74
p a): $n_{Os}$ [%]	0.139	1.275	6.377	19.107	29.133	26.722	13.418	3.448	0.342
p b): $n_{Os}$ [%]	0.137	1.259	6.319	19.010	29.099	26.797	13.509	3.485	0.347
p c): $n_{Os}$ [%]	0.151	1.359	6.665	19.585	29.286	26.345	12.974	3.270	0.320
p d): $n_{Os}$ [%]	1.116	5.923	17.165	29.808	26.339	14.002	4.075	0.607	0.035

**Table 4.3:** Distribution of the relative osmium ion number densities in percent as a function of the ionization degree  $j$  for a plasma temperature  $T = 0.9 \cdot 10^8$  K and four different plasma (p) compositions a), b), c), d), as described in section 2.4.

Ionization State $j$	71	72	73	74	75	76
p a): $n_{Os}$ [%]	0.006	0.108	0.824	12.662	51.472	34.928
p b): $n_{Os}$ [%]	0.006	0.107	0.821	12.642	51.458	34.965
p c): $n_{Os}$ [%]	0.005	0.089	0.673	10.281	60.960	27.992
p d): $n_{Os}$ [%]	0.061	0.588	2.584	22.802	53.223	20.739

**Table 4.4:** Distribution of the relative osmium ion number densities in percent as a function of the ionization degree  $j$  for a plasma temperature  $T = 3.48 \cdot 10^8$  K and four different plasma compositions p a), p b), p c), p d), as described in section 2.4.

We are interested in analyzing if the K- and L-shells of the osmium ions are vacant (so that free electrons can recombine in these shells). Our results confirm such free shells for the higher considered temperature  $T = 3.48 \cdot 10^8$  K. There, in general, only one bound electron remains, which is not enough to fill even one of both shells. The situation seems to be different for the lower limit of the possible s-process temperatures ( $T = 0.9 \cdot 10^8$  K). For the plasma configurations a), b) and c) there are in average nearly six bound electrons, for the configuration d) even nearly seven. However, a few stellar plasma environment considerations are due here. First of all, we need to refer to section 2.4, where we described that the s-process proceeds within the C-pocket of the He intershell. This means that configuration d), with its high hydrogen content, is most unlikely. Then, we point out that the considered  $^{187}\text{Os}$  is a rather heavy isotope that cannot be produced at the beginning of the s-process. Indeed, it is possible that during the third dredge-up such heavy isotopes are mixed below into the building C-pocket, so that only few neutron captures are required to form  $^{187}\text{Os}$ . But since lighter nuclei are more abundant, this is not very likely. More probable is that our considered ion forms late in time, when the C-pocket has already heated up, close to the next thermal pulse or to the start of stationary He-burning. The best description of the neutron capture process on  $^{187}\text{Os}$  must therefore be the one calculated in section 4.1.2.3 at  $T = 3 \cdot 10^8$  K, where  $\bar{j} = 75.0093$  and the K-shell as well as the L-shell are most likely free. Even for the other constellations there is a high probability for vacant K- and L-shells. In every case there are effectively zero bound electrons between the nucleus and the merging point  $x_0$ . Since the merging quantum mechanical solution was derived from the K-shell wave function, this indicates a free K-shell. We can also assume that the few remaining bound electrons are in highly excited states due to the high thermal energy and the continuum depression, which enhances the probability to find a completely or almost completely vacant L-shell, too. Even in their ground state the osmium ions would always have a vacant state in the L-shell. This result confirms the assumption in Ref. [Hel11] that effective NEEC of an osmium ion in a stellar plasma under s-process conditions is possible. In the following we double-check our calculation.

## 4.2 Comparison With Values From the Literature

In Ref. [TY83] also osmium ions in s-process plasma configurations were addressed and their ionization states calculated for various temperatures and two plasma compositions, corresponding to our plasma configurations c) and d), see section 2.4. The latter we included solely because of their usage in the literature for the classical s-process model. According to what we have shown in section 2.4, the plasma configurations of Ref. [TY83] deviate from the supposedly realistic s-process environment and have therefore only limited validity. However, we can use the data given to double-check our calculation method. For the temperatures considered in our work only plasma configuration c) was treated in Ref. [TY83] which therefore delivers our comparison case for  $T = 3 \cdot 10^8$  K. Their results for the osmium ionization states were presented graphically. For this reason, we are forced to reproduce their ionization distribution on the basis of their calculation method. Ref. [TY83] gave a numerical approximation for the continuum depression, derived from the finite temperature Fermi model, as a function of the temperature, the plasma electron number density and the ionization state  $j$  of the ion in question. They also assumed fully ionized He ions and the mass density  $\rho = 10^3 \text{g/cm}^3$ . Applying their method we receive their ionization distribution as confirmed by a comparison between Figure 4.4 (reproduced results) and Figure 7 in Appendix B of [TY83]. In a next step we calculate the ionization distribution using our method presented in chapter 3 with a rigorous treatment of the continuum depression (see section 3.3). Our results are illustrated as well in Figure 4.4 and show a very good agreement.

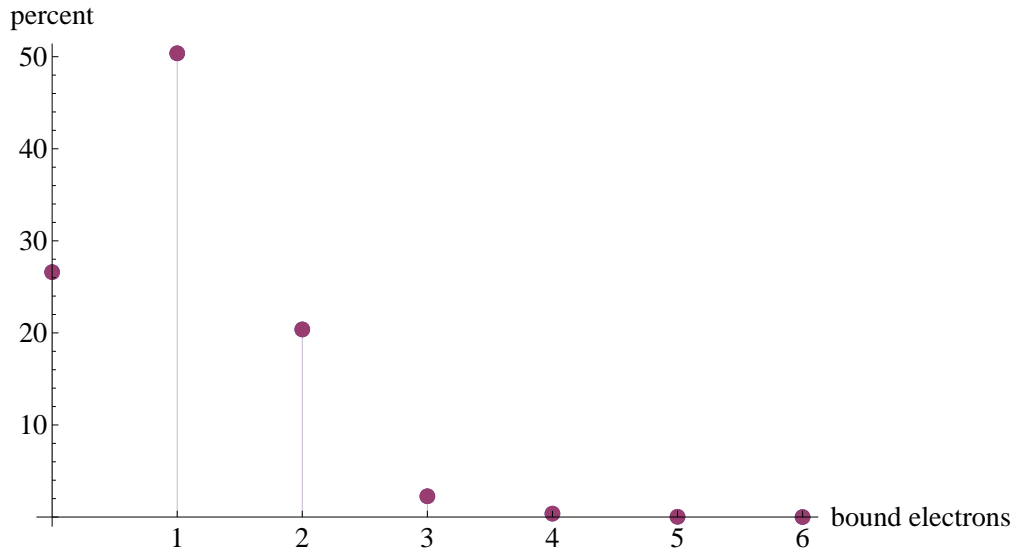


**Figure 4.4:** Relative abundances of Os ionic states (ion number densities in percent) in a pure helium plasma at temperature  $T = 3 \cdot 10^8$  K and mass density  $\rho = 10^3 \text{g/cm}^3$ . Blue dots (concealed by the red ones) result from the numerical approximation of the continuum depression described in [TY83], red dots illustrate our results. The abscissa shows the number of bound electrons.

As can be seen, there is no noticeable difference between both results. Only the Table 4.6 reveals deviations of less than 2/100 percent. This good agreement confirms the validity of our results.

Plasma Configuration	a)	b)	c)	d)
$T_8 = 0.9 : \bar{j}$	70.2877	70.2944	70.3109	69.3145
$T_8 = 3.48 : \bar{j}$	75.2027	75.2033	75.1608	74.9074

**Table 4.5:** Average ionization state of the osmium ion for two different plasma temperatures,  $T = 0.9 \cdot 10^8$  K and  $T = 3.48 \cdot 10^8$  K, and four different plasma compositions a), b), c), d), as described in section 2.4.  $T_8$  gives the temperature in units of  $10^8$  K.

Ionization State $j$	71	72	73	74	75	76
[TY83]: $n_{Os}$ [%]	0.027	0.370	2.257	20.376	50.362	26.607
Here: $n_{Os}$ [%]	0.027	0.368	2.254	20.379	50.379	26.590
[TY83]-Here [%]	0.000	0.002	0.003	-0.003	-0.017	0.017

**Table 4.6:** Relative abundances of Os ionic states (ion number densities in percent) in a pure helium plasma at temperature  $T = 3 \cdot 10^8$  K and mass density  $\rho = 10^3 \text{ g/cm}^3$ . We compare our results with the ones of Takahashi and Yokoi in [TY83].

# Summary and Outlook

## Summary

The aim of this thesis has been to investigate whether the atomic K- and L-shells of a heavy ion in a stellar plasma under s-process conditions are unoccupied. This goal was formulated within the framework of an investigation on the impact of nuclear excitation by electron capture (NEEC) on highly excited nuclear states directly after neutron capture. Especially the L-shell electron capture has a noticeable effect on the nuclear decay modes ratio, followed to a lesser extent by capture into the K-shell. It was therefore essential to know if the electron can be captured into the K- and L-shells of the respective isotope. To this end we have adopted osmium as a model ion and calculated its ionization states in the corresponding plasma with the help of the Saha equation.

To obtain plasma configurations which constitute a realistic environment for the respective process we have investigated the stellar development that leads to the formation of s-process isotopes. We have identified the C pocket as the most likely physical site with its main components helium, carbon and osmium and temperatures between  $0.9 \cdot 10^8$  K and  $3 \cdot 10^8$  K. These plasma conditions we have adopted for our calculation. We have also chosen two additional plasma compositions and an even higher temperature of  $3.48 \cdot 10^8$  K to cover traditional assumptions of s-process sites and allow for a comparison with values from the literature. With the obtained parameters for four plasma configurations and the mentioned temperatures we have calculated the ionization states via the Saha equation. The detailed step-by-step calculation has been presented for one model case.

The surrounding particles of the plasma had to be taken into account. They cause a reduction of the binding energies for the bound electrons of the osmium ion, even leading to additional pressure ionization. This so-called continuum depression we have handled within a Fermi model, partly adjusted to account for quantum mechanical features in the vicinity of the considered nucleus. Within this model, various approximations have been implemented to effectively compute the nuclear potential. Especially the regions close to and very far from the nucleus needed special considerations. The nuclear potential we have used to calculate the influence of the perturbing potential of the plasma particles in a self-consistent way, finally leading to the value for the continuum depression energy. By subtracting this energy from the laboratory value for the ionization potentials of osmium we have also obtained the cut-off energy for the considered excitation energies. Only those excitation states which not compete against ionization are included in the partition functions of the Saha equation.

With the evaluated ingredients we finally have obtained ionization distributions for osmium that bear comparison with the literature and show clearly that there are not enough bound electrons left to fill the K- and L-shells of the ions. The average bound electron number ranges between one and a maximum of seven. The unoccupied states provide the condition for effective NEEC to occur which therefore seems to stay a subject for continuing research.



## Outlook

The present calculation offers some possibilities for refinement. Instead of applying the same quantum mechanical correction in the relativistic as in the non-relativistic case, a fully relativistic treatment might increase the accuracy of the results. The same is true for taking into account a more detailed composition of the plasma and including even the rare components.

In the framework of NEEC there is also room for further investigation. So far we have studied the occupation of the K- and L-shells of osmium to see whether NEEC in those shells is possible as proposed in Ref. [Hel11]. Another unverified assumption there was that if capture occurs into the L-shell, the K-shell or even orbitals of the L-shell would be fully occupied. With our calculation we showed the opposite. There is a high probability for the K-shell to be free in any case. The effect of the free underlying shell on the decay modes should therefore be investigated. Furthermore, the few remaining bound electrons might partly occupy the L-shell and couple to the captured electron. Such coupling has not been considered so far, since in Ref. [Hel11] only completely occupied orbitals with total angular momentum zero were assumed. The impact of NEEC on nucleosynthesis scenarios for various electronic configurations can be investigated. This opens an ample field for further studies.

# Bibliography

- [AGB12] Asymptotic giant branch (AGB) stars, <http://www.noao.edu/outreach/press/pr03/sb0307.html>, 2012.
- [AH70] N. Ashby and M. A. Holzman. Semistatistical model for electrons in atoms. *Phys. Rev. A*, 1:764–777, Mar 1970.
- [AS64] M. Abramowitz and I. A. Stegun. *Handbook of Mathematical Functions with Formulas, Graphs, and Mathematical Tables*. Dover, New York, 9th dover printing edition, 1964.
- [BBB<sup>+</sup>] L. A. Bernstein, D. L. Bleuel, C. R. Brune, R. D. Hoffman, I. Y. Lee, L. Phair, and D. H. G. Schneider. Interactions between highly excited nuclei and photons in astrophysical plasmas. unpublished.
- [BBFH57] E. M. Burbidge, G. R. Burbidge, W. A. Fowler, and F. Hoyle. Synthesis of the elements in stars. *Rev. Mod. Phys.*, 29:547–650, Oct 1957.
- [BBK<sup>+</sup>00] Z. Y. Bao, H. Beer, F. Käppeler, F. Voss, K. Wisshak, and T. Rauscher. Neutron cross sections for nucleosynthesis studies. *Atomic Data and Nuclear Data Tables*, 76(1):70–154, 2000.
- [BFF<sup>+</sup>96] F. Bosch, T. Faestermann, J. Friese, F. Heine, P. Kienle, E. Wefers, K. Zeitelhack, K. Beckert, B. Franzke, O. Klepper, et al. Observation of bound-state  $\beta^-$  decay of fully ionized  $^{187}\text{Re}$ :  $^{187}\text{Re}$ - $^{187}\text{Os}$  cosmochronometry. *Phys. Rev. Lett.*, 77:5190–5193, 1996.
- [Bra08] H. Bradt. *Supplement to Chapter 4 of Astrophysical Processes (AP)*. Cambridge Univ. Press, Cambridge, 2008.
- [BS88] A. I. Boothroyd and I.-J. Sackmann. Low-mass stars. III. low-mass stars with steady mass loss: Up to the asymptotic giant branch and through the final thermal pulses. *The Astrophysical Journal*, 328:653–670, 1988.
- [CG68] J. P. Cox and R. T. Giuli. *Principles of Stellar Structure: Physical Principles*. Gordon and Breach, 1968.
- [Cla64] D. D. Clayton. Cosmoradiogenic chronologies of nucleosynthesis. *The Astrophysical Journal*, 139:637, 1964.
- [CSG<sup>+</sup>09] S. Cristallo, O. Straniero, R. Gallino, L. Piersanti, I. Domínguez, and M. T. Lederer. Evolution, nucleosynthesis, and yields of low-mass asymptotic giant branch stars at different metallicities. *The Astrophysical Journal*, 696:797, 2009.
- [FMM<sup>+</sup>10] K. Fujii, M. Mosconi, A. Mengoni, C. Domingo-Pardo, F. Käppeler, U. Abbondanno, G. Aerts, H. Álvarez-Pol, F. Álvarez-Velarde, S. Andriamonje, et al. Neutron physics of the Re/Os clock. III. Resonance analyses and stellar (n, $\gamma$ ) cross sections of  $^{186,187,188}\text{Os}$ . *Phys. Rev. C*, 82:015804, Jul 2010.
- [FMT49] R. P. Feynman, N. Metropolis, and E. Teller. Equations of state of elements based on the generalized Fermi-Thomas theory. *Phys. Rev.*, 75(10):1561–1573, 1949.

- [GAB<sup>+</sup>98] R. Gallino, C. Arlandini, M. Busso, M. Lugaro, C. Travaglio, O. Straniero, A. Chieffi, and M. Limongi. Evolution and nucleosynthesis in low-mass asymptotic giant branch stars. II. neutron capture and the s-process. *The Astrophysical Journal*, 497(1):388, 1998.
- [GM04] G. Gosselin and P. Morel. Enhanced nuclear level decay in hot dense plasmas. *Phys. Rev. C*, 70:064603, Dec 2004.
- [GMM07] G. Gosselin, V. Méot, and P. Morel. Modified nuclear level lifetime in hot dense plasmas. *Phys. Rev. C*, 76:044611, Oct 2007.
- [GMM10] G. Gosselin, P. Morel, and P. Mohr. Modification of nuclear transitions in stellar plasma by electronic processes: *K* isomers in <sup>176</sup>Lu and <sup>180</sup>Ta under s-process conditions. *Phys. Rev. C*, 81:055808, May 2010.
- [Hel11] S. Helmrich. *Nuclear Excitation by Electron Capture in Stellar Environments*. Bachelor’s thesis, Universität Heidelberg, 2011.
- [Her05] F. Herwig. Evolution of asymptotic giant branch stars. *Annual Review of Astronomy and Astrophysics*, 43(1):435–479, 2005.
- [Ili07] C. Iliadis. *Nuclear Physics of Stars*. Physics Textbook. Wiley-VCH, 2007.
- [JH06] G. Job and F. Herrmann. Chemical potential—a quantity in search of recognition. *European Journal of Physics*, 27:353, 2006.
- [KBW89] F. Käppeler, H. Beer, and K. Wisshak. s-process nucleosynthesis-nuclear physics and the classical model. *Reports on Progress in Physics*, 52(8):945, 1989.
- [KGBA11] F. Käppeler, R. Gallino, S. Bisterzo, and W. Aoki. The s process: Nuclear physics, stellar models, and observations. *Rev. Mod. Phys.*, 83(1):157–193, Apr 2011.
- [KK88] N. Klay and F. Käppeler.  $\beta$ -decay rate of <sup>79m</sup>Se and its consequences for the s-process temperature. *Phys. Rev. C*, 38:295–306, Jul 1988.
- [LLP80] L. D. Landau, E. M. Lifšic, and L. P. Pitaevskij. *Statistical Physics: Course of Theoretical Physics*. Pergamon Press, 1980.
- [MFM<sup>+</sup>10] M. Mosconi, K. Fujii, A. Mengoni, C. Domingo-Pardo, F. Käppeler, U. Abbondanno, G. Aerts, H. Álvarez-Pol, F. Álvarez-Velarde, S. Andriamonje, et al. Neutron physics of the Re/Os clock. I. Measurement of the (n, $\gamma$ ) cross sections of <sup>186,187,188</sup>Os at the CERN n\_TOF facility. *Phys. Rev. C*, 82:015802, Jul 2010.
- [Mor82] R. M. More. Electronic energy-levels in dense plasmas. *Journal of Quantitative Spectroscopy and Radiative Transfer*, 27(3):345–357, 1982.
- [MTN08] P. J. Mohr, B. N. Taylor, and D. B. Newell. Codata recommended values of the fundamental physical constants: 2006. *Rev. Mod. Phys.*, 80(2):633–730, Jun 2008.
- [MVR95] J. A. Miralles and K. A. Van Riper. Accurate evaluation of fermi-dirac integrals and their derivatives for arbitrary degeneracy and relativity. *The Astrophysical Journal Supplement Series*, 105:407, 1995.
- [OLBC10] F. W. J. Olver, D. W. Lozier, R. F. Boisvert, and C. W. Clark, editors. *NIST Handbook of Mathematical Functions*. Cambridge University Press, 1 edition, 2010.
- [Ols61] H. N. Olsen. Partition function cutoff and lowering of the ionization potential in an argon plasma. *Phys. Rev.*, 124:1703–1708, Dec 1961.

- [Pó6] A. Pálffy. *Theory of nuclear excitation by electron capture for heavy ions*. PhD thesis, Universität Gießen, 2006.
- [PSH06] A. Pálffy, W. Scheid, and Z. Harman. Theory of nuclear excitation by electron capture for heavy ions. *Phys. Rev. A*, 73(1):012715, Jan 2006.
- [Sah20] M. N. Saha. Ionization in the solar chromosphere. *Philosophical Magazine Series*, 1920.
- [Son04] K. Sonnabend. *Untersuchung von "branching points" im astrophysikalischen s-Prozess mit reellen Photonen*. PhD thesis, Technische Universität Darmstadt, 2004.
- [Spe12] Atomic database spectr-w<sup>3</sup> for plasma spectroscopy and other applications, <http://spectr-w3.snz.ru/ion.phtml>, 2012.
- [SPJ66] J. C. Stewart and K. D. Pyatt Jr. Lowering of ionization potentials in plasmas. *The Astrophysical Journal*, 144:1203, 1966.
- [SUM<sup>+</sup>05] T. Shizuma, H. Utsunomiya, P. Mohr, T. Hayakawa, S. Goko, A. Makinaga, H. Akimune, T. Yamagata, M. Ohta, H. Ohgaki, et al. Photodisintegration cross section measurements on <sup>186</sup>W, <sup>187</sup>Re, and <sup>188</sup>Os: Implications for the re-os cosmochronology. *Phys. Rev. C*, 72:025808, 2005.
- [Tak98] K. Takahashi. The <sup>187</sup>Re - <sup>187</sup>Os cosmochronometry—the latest developments. *AIP Conference Proceedings*, 425(1):616–625, 1998.
- [TY83] K. Takahashi and K. Yokoi. Nuclear  $\beta$ -decays of highly ionized heavy atoms in stellar interiors. *Nuclear Physics A*, 404(3):578 – 598, 1983.
- [VGK94] V. S. Volokitin, I. O. Golosnoi, and N. N. Kalitkin. Wide-range equation of state of matter. I. analysis of nonideality models. *Russian Physics Journal*, 37(11):1029–1047, 1994.

# Acknowledgements

Mein herzlicher Dank gilt allen, die mir das Anfertigen dieser Arbeit ermöglichten.

Zuallererst bedanke ich mich bei Herrn Prof. Christoph Keitel, der mich so freundlich am MPI aufnahm und mir damit die Möglichkeit gab, das motivierende Arbeiten in einer Arbeitsgruppe kennenzulernen.

Aus tiefstem Herzen bedanke ich mich bei Frau Dr. Adriana Pálffy, die mich nicht nur in das Thema einführte und meiner Arbeit ein Ziel gab, sondern auch stets und vor allem in der harten Endphase der Arbeit viel Zeit für mich opferte und mir mit Rat, Tat und aufmunternden Worten fachlich sowie freundschaftlich zur Seite stand. Besonders hilfreich für mich waren ihre Verbesserungsvorschläge, ohne die meine Arbeit in dieser Form nicht hätte entstehen können. Ich danke ihr für die vielen Dinge, die ich im Laufe der Arbeit von ihr lernen konnte.

Ein ganz besonderer und tief empfundener Dank geht an Sebastian Meuren, der mir mit seinem Wissen zum Fermi Modell über eine kritische Phase hinweghalf, immer selbstlos und bereitwillig Fragen beantwortete und mir seine Hilfe stets anbot.

Ich danke auch Stephan Helmrich sehr, der bei mir auftretende Fragen zu seiner Bachelorarbeit klärte und mir so den Einstieg in die Thematik erleichterte.

Ferner danke ich all denjenigen aus der Abteilung, die mir bei Computerproblemen im Allgemeinen und Mathematicaproblemen im Besonderen weiterhalfen, hierunter zu nennen sind insbesondere Stefano Cavaletto, Anton Wöllert und Michael Klaiber. Ich möchte meinen Dank auch den Kollegen aussprechen, die mit mir das Büro teilten und für die warmherzige Atmosphäre sorgten, die mir ein schönes Arbeitsumfeld bereitete. Ebensolchen Dank hat Sibel Babacan verdient, die administrative Angelegenheiten für mich regelte.

An dieser Stelle geht auch ein dickes Dankeschön an meine Familie, die mir stets den Rücken stärkt und immer für mich da ist. Ich verdanke ihr alles.

Nicht zuletzt bedanke ich mich bei Axel, der die letzten Jahre geduldig und nachsichtig an meiner Seite stand und den ich sehr liebe.

# Erklärung

Ich versichere, dass ich diese Arbeit selbstständig verfasst und keine anderen als die angegebenen Quellen und Hilfsmittel benutzt habe.

Heidelberg, den 09.04.2012